

First broadband characterization and redshift determination of the VHE blazar MAGIC J2001+439

J. Aleksić¹, S. Ansoldi², L. A. Antonelli³, P. Antoranz⁴, A. Babic⁵, P. Bangale⁶, U. Barres de Almeida⁶, J. A. Barrio⁷, J. Becerra González^{8,25,*}, W. Bednarek⁹, E. Bernardini¹⁰, A. Biland¹¹, O. Blanch¹, S. Bonnefoy⁷, G. Bonnoli³, F. Borracci⁶, T. Bretz^{12,26}, E. Carmona¹³, A. Carosi³, D. Carreto Fidalgo⁷, P. Colin⁶, E. Colombo⁸, J. L. Contreras⁷, J. Cortina¹, S. Covino³, P. Da Vela⁴, F. Dazzi⁶, A. De Angelis², G. De Caneva¹⁰, B. De Lotto², C. Delgado Mendez¹³, M. Doert¹⁴, A. Domínguez^{15,27}, D. Dominis Prester⁵, D. Dorner¹², M. Doro¹⁶, S. Einecke¹⁴, D. Eisenacher¹², D. Elsaesser¹², E. Farina¹⁷, D. Ferenc⁵, M. V. Fonseca⁷, L. Font¹⁸, K. Frantzen¹⁴, C. Fruck⁶, R. J. García López⁸, M. Garczarczyk¹⁰, D. Garrido Terrats¹⁸, M. Gaug¹⁸, N. Godinovic⁵, A. González Muñoz¹, S. R. Gozzini¹⁰, D. Hadasch¹⁹, M. Hayashida²⁰, J. Herrera⁸, A. Herrero⁸, D. Hildebrand¹¹, J. Hose⁶, D. Hrupec⁵, W. Idec⁹, V. Kadenius²¹, H. Kellermann⁶, K. Kodani^{20,*}, Y. Konno²⁰, J. Krause⁶, H. Kubo²⁰, J. Kushida²⁰, A. La Barbera³, D. Lelas⁵, N. Lewandowska¹², E. Lindfors^{21,28}, S. Lombardi³, M. López⁷, R. López-Coto¹, A. López-Oramas¹, E. Lorenz⁶, I. Lozano⁷, M. Makariev²², K. Mallot¹⁰, G. Maneva²², N. Mankuzhiyil², K. Mannheim¹², L. Maraschi³, B. Marcote²³, M. Mariotti¹⁶, M. Martínez¹, D. Mazin⁶, U. Menzel⁶, M. Meucci⁴, J. M. Miranda⁴, R. Mirzoyan⁶, A. Moralejo¹, P. Munar-Adrover²³, D. Nakajima²⁰, A. Niedzwiecki⁹, K. Nilsson^{21,28}, K. Nishijima²⁰, K. Noda⁶, N. Nowak⁶, R. Orito²⁰, A. Overkemping¹⁴, S. Paiano¹⁶, M. Palatiello², D. Paneque^{6,*}, R. Paoletti⁴, J. M. Paredes²³, X. Paredes-Fortuny²³, S. Partini⁴, M. Persic^{2,29}, F. Prada^{15,30}, P. G. Prada Moroni²⁴, E. Prandini¹¹, S. Preziuso⁴, I. Puljak⁵, R. Reinthal²¹, W. Rhode¹⁴, M. Ribó²³, J. Rico¹, J. Rodríguez García⁶, S. Rügemer¹², A. Saggion¹⁶, T. Saito²⁰, K. Saito²⁰, K. Satalecka⁷, V. Scalzotto¹⁶, V. Scapin⁷, C. Schultz¹⁶, T. Schweizer⁶, S. N. Shore²⁴, A. Sillanpää²¹, J. Sitarek¹, I. Snidarić⁵, D. Sobczynska⁹, F. Spanier¹², V. Stamatescu¹, A. Stamerra³, T. Steinbring¹², J. Storz¹², M. Strzys⁶, S. Sun⁶, T. Surić⁵, L. Takalo²¹, H. Takami²⁰, F. Tavecchio³, P. Temnikov²², T. Terzić⁵, D. Tescaro⁸, M. Teshima⁶, J. Thaele¹⁴, O. Tibolla¹², D. F. Torres¹⁹, T. Toyama⁶, A. Treves¹⁷, M. Uellenbeck¹⁴, P. Vogler¹¹, R. M. Wagner^{6,31}, F. Zandanel^{15,32}, R. Zanin²³, (*The MAGIC Collaboration*), F. D'Ammando^{33,34}, T. Hovatta³⁵, V. M. Larionov^{36,37,38}, W. Max-Moerbeck³⁹, M. Perri^{3,40}, A. C. S. Readhead³⁵, J. L. Richards⁴¹, T. Sakamoto⁴², R. D. Schwartz^{43,45}, F. Verrecchia⁴⁰, and L.C. Reyes⁴⁴

(Affiliations can be found after the references)

Received ... ; accepted ...

ABSTRACT

Aims. We aim to characterize the broadband emission from 2FGL J2001.1+4352, which has been associated with the unknown-redshift blazar MG4 J200112+4352. Based on its gamma-ray spectral properties, it was identified as a potential very high energy (VHE; $E > 100$ GeV) gamma-ray emitter. We investigate whether this object is a VHE emitter, characterize its gamma-ray spectrum, and study the broadband emission within the one-zone synchrotron self-Compton (SSC) scenario, which is commonly used to describe the emission in blazars. Moreover, we also intend to determine the redshift of this object, which is a crucial parameter for its scientific interpretation.

Methods. The source was observed with MAGIC first in 2009 and later in 2010 within a multi-instrument observation campaign. The MAGIC observations yielded 14.8 hours of good quality stereoscopic data. Besides MAGIC, the campaign involved, observations with *Fermi*-LAT, *Swift*-XRT/UVOT, the optical telescopes KVA, Goddard Robotic Telescope, Galaxy View observatory, Crimean Astrophysical observatory, St. Petersburg observatory, and the Owens Valley Radio Observatory. The object was monitored at radio, optical and gamma-ray energies during the years 2010 and 2011. We characterize the radio to VHE spectral energy distribution and quantify the multiband variability and correlations over short (few days) and long (many months) timescales. We also organized deep imaging optical observations with the Nordic Optical Telescope in 2013 to determine the source redshift.

Results. The source, named MAGIC J2001+439, is detected for the first time at VHE with MAGIC at a statistical significance of 6.3σ ($E > 70$ GeV) during a 1.3-hour long observation on 2010 July 16. The multi-instrument observations show variability in all energy bands with the highest amplitude of variability in the X-ray and VHE bands. Besides the variability on few-day timescales, the long-term monitoring of MAGIC J2001+439 shows that, the gamma-ray, optical, and radio emissions gradually decreased on few-month timescales from 2010 through 2011, indicating that at least some of the radio, optical and gamma-ray emission is produced in a single region by the same population of particles. We also determine for the first time the redshift of this BL Lac object through the measurement of its host galaxy during low blazar activity. Using the observational evidence that the luminosities of BL Lac host galaxies are confined to a relatively narrow range, we obtain $z = 0.18 \pm 0.04$. Additionally, we use the *Fermi*-LAT and MAGIC gamma-ray spectra to provide an independent redshift estimation, $z = 0.17 \pm 0.10$. Using the former (more accurate) redshift value, we adequately describe the broadband emission with a one-zone SSC model for different activity states and interpret the few-day timescale variability as produced by changes in the high-energy component of the electron energy distribution.

Key words. Galaxies: active – BL Lac objects: individual (MAGIC J2001+439) – gamma rays: observations

1. Introduction

Blazars are radio-loud active galactic nuclei (AGN) with relativistic jets pointing towards the observer (see e.g. Urry & Padovani 1995). They are the most common extragalactic sources detected in the very high energy (VHE; $E > 100$ GeV) gamma-ray range. The spectral energy distributions (SEDs) of blazars show a double-bump shape. The first bump peaks at optical/X-ray frequencies and is attributed to synchrotron radiation from relativistic electrons. On the other hand, the origin of the second bump, which peaks at gamma-ray energies, is still under debate. Leptonic models are generally favored. In these models, the high-energy (HE; $E > 100$ MeV) radiation is produced by inverse Compton (IC) of primary HE electrons scattering off low-energy photons. The origin of target low-energy photons may be synchrotron radiation of the primary electrons themselves in the synchrotron self-Compton (SSC) scenario (Band & Grindlay 1985; Maraschi et al. 1992; Bloom & Marscher 1996), or seed photons produced outside of the jet in the external Compton (EC) scenario (Dermer & Schlickeiser 1993; Sikora et al. 1994). However, hadron-driven emission is also possible (e.g. Mannheim & Biermann 1992; Mücke et al. 2003). The emission would include proton, muon, and pion synchrotron radiation, as well as production of gamma rays from neutral pion decays, electrons, and positrons generated in charged pion decays that result from photon-hadron collisions. The hadronic models require total jet powers that are typically about 1-2 orders of magnitude higher than for the leptonic models.

Blazars are separated into two categories by the equivalent widths of their optical emission lines, BL Lac objects and flat-spectrum radio quasars (FSRQs). The BL Lac objects show featureless optical spectra with weak or no emission lines that are possibly masked by a strong non-thermal emission from the relativistic jet, while the FSRQs display prominent broad emission lines in their optical spectra. The absence of emission/absorption lines makes it very difficult to determine the redshift for distant BL Lac objects, which often precludes detailed studies on the nature, intrinsic characteristics of individual objects, and substantially hampers and/or biases blazar population/unification studies.

The flux of the VHE gamma-ray photons coming from a distant source is attenuated by electron-positron pair creation due to interaction with the extragalactic background light (EBL; Gould & Schréder 1966; Stecker 1969; Fazio & Stecker 1970; Hauser & Dwek 2001). The EBL is the sum of the stellar and dust emission integrated over cosmic time. The EBL photon density carries information about the cosmic history of the star formation rate on galaxy evolution. Several EBL models have been proposed in the past few years (Stecker et al. 2006; Franceschini et al. 2008; Gilmore et al. 2009; Kneiske & Dole 2010; Finke et al. 2010; Domínguez et al. 2011). The VHE gamma-ray absorption is energy dependent and increases strongly with redshift. Therefore, the observed VHE spectra from distant sources are distorted with respect to the intrinsic source spectra. The distances of unknown redshift BL Lac objects can be estimated by comparing the GeV and TeV spectra and assuming a specific EBL model (Prandini et al. 2011). This estimation is based on the measurement of the intrinsic source spectrum with the *Fermi* Large Area Telescope (LAT) at energies below ~ 10 -30 GeV, where there is little or no EBL absorption.

There are only ~ 50 blazars significantly detected at VHE¹. This very low number of known VHE blazars is a consequence of the difficulty of performing sensitive scans over large portions of the sky with Imaging Atmospheric Cherenkov Telescopes (IACTs), which have narrow field of view (3° - 5°) cameras and only ~ 1000 hours of moonless time per year with good weather conditions. On the other hand, more than 1000 HE

gamma-ray emitting blazars have been detected with *Fermi*-LAT (Abdo et al. 2009; Nolan et al. 2012), and many of them have been identified (based on their spectral properties) as potential VHE emitting sources (Ackermann et al. 2013).

The object 0FGL J2001.0+4352 was initially one of the unidentified *Fermi*-LAT sources included in the *Fermi* bright source list (Abdo et al. 2009). This source was first detected only above 1 GeV with a photon flux $F_{1\text{GeV}} = (7.8 \pm 1.2) \times 10^{-9}$ ph cm⁻² s⁻¹ between 1 and 100 GeV. Early on, this source was identified by the *Fermi*-LAT collaboration as a source expected to exhibit VHE emission, which is information that was shared with the H.E.S.S., MAGIC and VERITAS collaborations in 2009 October. This information triggered observations with MAGIC, which led to the first VHE detection of this source in 2010 July (see Mariotti et al. 2010; Berger et al. 2010, 2011). This source was initially designated MAGIC J2001+435, although we change its name to MAGIC J2001+439 in this paper to properly follow the IAU guidelines for naming astronomical objects.

The latest *Fermi*-LAT catalogs confirmed the brightness and hardness of the gamma-ray spectra of this source. In the second *Fermi*-LAT source catalog (2FGL, Nolan et al. 2012), this source is denoted 2FGL J2001.1+4352, and its spectrum is characterized with a power-law function $dN/dE \propto E^{-\Gamma}$ with $\Gamma = 1.90 \pm 0.03$ above 100 MeV. This source is also present in the first *Fermi* HE LAT catalog (1FHL, Ackermann et al. 2013), where it is denoted 1FHL J2001.1+4353, and the spectrum is characterized by a power-law function with $\Gamma = 2.38 \pm 0.18$ above 10 GeV, extending to VHE with a flux above 100 GeV of $F_{100\text{GeV}} = (2.2^{+1.9}_{-1.2}) \times 10^{-11}$ ph cm⁻² s⁻¹ (Ackermann et al. 2013). Bassani et al. (2009) found a counterpart consistent with the radio bright source MG4 J200112+4352² from the NRAO VLA Sky Survey (NVSS; Condon et al. 1998) 20 cm wavelength image. The object MG4 J200112+4352 is only 0.01 deg away from the location of 2FGL J2001.1+4352 (which has a 95% confidence level position uncertainty of 0.02 deg) and is consistent with the *Swift* and the XMM Slew positions in the X-ray band. The source was identified as a BL Lac object using spectroscopic observations with the 1.52 m optical telescope from the Bologna Astronomical observatory and was classified as a high-frequency-peaked BL Lac object (HBL) by Bassani et al. (2009). The source redshift remained undetermined due to the low signal-to-noise ratio of their observations. Yet, they found indications of a slope change in the optical spectrum, which could be interpreted as a non-thermal component merging with the light from the host galaxy. Based on this feature, they gave a rough estimate of ~ 0.2 for the redshift of this source. More recently, Shaw et al. (2013) used higher quality optical observations to derive a lower limit for the redshift of $z > 0.11$, based on the non-detection of the host galaxy, which was assumed to be a giant elliptical galaxy with an absolute R-band magnitude of $M_R = -22.5 \pm 0.5$.

In this paper, we report the results from a multi-wavelength (MWL) campaign from summer 2010, providing coverage from the radio up to the VHE gamma-ray band and leading to the first VHE detection of this source. The multi-instrument observations allowed us to characterize, the radio to VHE broadband SED of this object for the first time. We also report on the multi-band variability and correlation properties during this campaign and follow-up observations performed during the years 2010 and 2011. Moreover, we report the first measurement of the redshift for this source through the detection of its host galaxy with the 2.5m Nordic Optical Telescope (NOT) during low blazar activity. Additionally, we also estimate the redshift of this object using the HE and VHE gamma-ray spectra, as measured by *Fermi*-LAT and MAGIC. We then use the measured SED and redshift information to characterize the radio to VHE broadband emis-

² MG4 J200112+4352 is located at RA(J2000) = 20h 01m 12.9s, Dec(J2000) = +43d 52m 53s (NASA/IPAC Extragalactic Database, <http://ned.ipac.caltech.edu>).

¹ <http://tevcat.uchicago.edu>

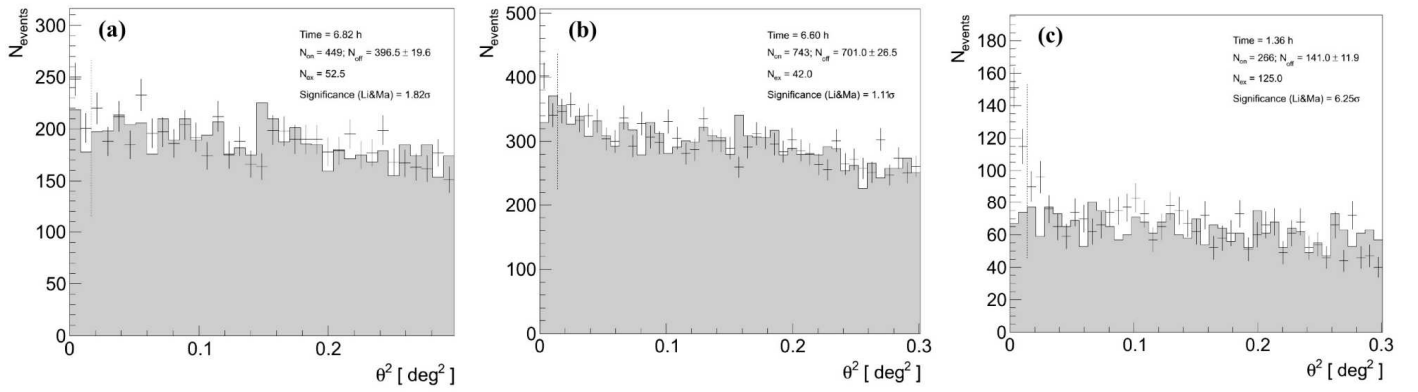


Fig. 1. Theta-squared distributions of MAGIC J2001+439 observed on 2009 November (panel (a), energy threshold is $E > 100$ GeV) between July and September excluding 2010 July 16 (panel (b), $E > 70$ GeV) and on 2010 July 16 (panel (c), $E > 70$ GeV). Crosses represent the event distribution from the source, while the gray histogram the measured background. The signal region is indicated by the vertical dotted line.

sion within a standard one-zone SSC scenario and investigate the origin of the detected variability. In this paper, we assume cosmological parameters $H_0 = 67 \text{ km s}^{-1} \text{ Mpc}^{-1}$, $\Omega_m = 0.315$, $\Omega_\Lambda = 0.685$ (Ade et al. 2013).

2. MAGIC observations and results

2.1. Observation and data analysis

The MAGIC stereoscopic system consists of two IACTs with a mirror dish diameter of 17 m located at the Roque de los Muchachos, La Palma in Canary Island (28.8°N, 17.8°W at 2200 m a.s.l.). The MAGIC telescopes have been operating in stereoscopic mode since autumn 2009, which provided integral sensitivity of 0.76% of the Crab Nebula flux above 300 GeV for 50 hour observation time (Aleksić et al. 2012).

The object MAGIC J2001+439 was observed between 2009 November 7 and 26 for a total of 9.0 hours. The MAGIC observations were also performed in a MWL campaign between 2010 July 6 and September 8 for a total of 14.4 hours. The data were taken with zenith angles in the range 20 deg – 40 deg in 2009 November and with zenith angles in the range 15 deg – 30 deg during the campaign in 2010 July – September. The observations were carried out in wobble mode (Fomin et al. 1994), where the target source position has an offset of 0.4° from the camera center. The direction of the wobble offset between two symmetric sky locations is alternated every 20 minutes to minimize systematic errors originating from possible exposure inhomogeneities.

The data were analyzed using the standard analysis chain (Aleksić et al. 2012) with the MAGIC Analysis and Reconstruction Software (MARS; Moralejo et al. 2009; Zanin et al. 2013). Camera images were cleaned using a sum image-cleaning method (Lombardi et al. 2011; Zanin 2011). This algorithm originated from the concept of the sum trigger (Rissi 2009; Haefner et al. 2011). In this procedure, the signals are clipped in amplitude and all possible combinations of 2, 3 and 4 neighboring pixels in the camera are summed up. If the sum of the charges is above a certain threshold within a short time interval, these pixels are considered to belong to the shower image. The clipping ensures that afterpulses or strong night sky background fluctuations do not dominate the summed pixels. Generally, the sum image-cleaning method recovers more pixels than the standard method. This is important for reconstructing shower images of low-energy gamma rays.

2.2. Results

Figure 1 shows the distribution of the squared angular distance (θ^2) between the reconstructed arrival directions of the events and the real source position in the camera.

We found an excess of events $N_{ex} = 125.0 \pm 20.2$ in the energy range above 70 GeV in the observation on 2010 July 16 in which the effective observation time was 1.36 hours (see Figure 1 (c)). This gamma-ray excess yields a signal significance of 6.3σ calculated using Eq.17 of Li & Ma (1983). When correcting for the seven observations (trials) performed in the MWL campaign, we find a post-trial signal significance of 6.0σ , hence implying the first detection of VHE gamma rays from 2FGL J2001.1+4352. The time-averaged integral photon flux above 200 GeV corresponds to $\sim 9\%$ of the Crab Nebula flux. The detected position of the excess (RA(J2000): 20.021 ± 0.001 h, Dec(J2000): $43.879 \pm 0.010^\circ$) is consistent with the position of 2FGL J2001.1+4352³ within 0.02° . The distribution of the gamma-ray excess is consistent with a point-like source. The source was not detected during the rest of the observing campaign (see Figure 1 (b)). In the data between 2010 July and September (excluding 2010 July 16), the significance of the excess in 8.0 hours of observations is 1.1σ above the energy threshold of 70 GeV. Including the observations from 2010 July 16, the significance (above 70 GeV) of the accumulated dataset is 4σ . The data collected in 2009 November led to 6.8 hours of effective observation time, where we measure a gamma-ray excess above the energy threshold of 100 GeV at a significance level of 1.8σ (see Figure 1 (a)). The slightly higher energy threshold in the 2009 MAGIC observations with respect to that of the 2010 observations is due to the different zenith angle range for these two sets of observations.

The differential spectrum from the flare on 2010 July 16 can be described by a simple power law:

$$\frac{dN}{dE} = f_0 \times \left(\frac{E}{200 \text{ GeV}} \right)^{-\Gamma} \quad (1)$$

with flux normalization $f_0 = (1.9 \pm 0.4) \times 10^{-10} \text{ cm}^{-2} \text{ s}^{-1} \text{ TeV}^{-1}$ and photon index $\Gamma = 2.8 \pm 0.4$. The spectrum is fitted by a power-law function between 78 and 500 GeV. The systematic uncertainties in the spectral measurements with MAGIC stereo observations are 11% in the normalization factor (at 300 GeV) and 0.15-0.20 in the photon index. The error on the flux does not include uncertainty on the energy scale. The energy scale of the MAGIC telescopes is determined with a precision of about 17% at low energies ($E < 100$ GeV) and 15% at medium energies ($E > 300$ GeV). Further details are reported in Aleksić et al. (2012). We corrected for our limited energy resolution and energy bias using the Tikhonov unfolding algorithm (Albert et al. 2007). The result is shown in Figure 2.

³ 2FGL J2001.1+4352 is located at RA(J2000) = 20.019 h, Dec(J2000) = 43.879° in the 2FGL catalog (Nolan et al. 2012).

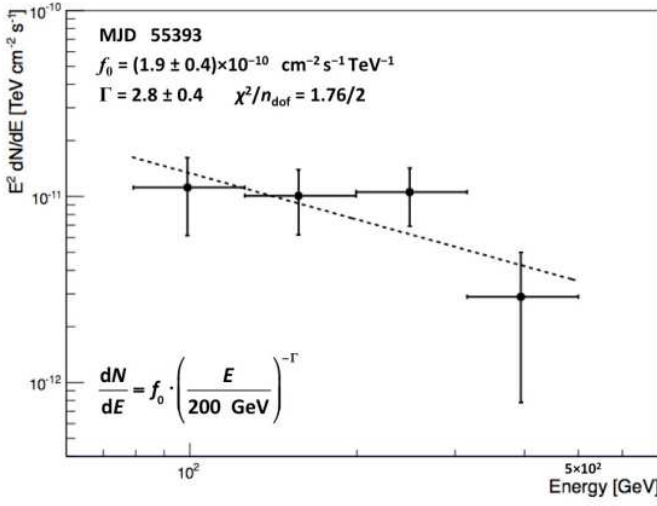


Fig. 2. VHE differential energy spectrum of MAGIC J2001+439 observed on 2010 July 16 with the MAGIC stereo system. The parameter values from the power-law fit are reported in the legend.

3. Multiband variability and correlations

3.1. Instrumentation and data analysis

3.1.1. *Fermi*-LAT

The *Fermi*-LAT is a pair conversion telescope designed to cover the energy band from 20 MeV to values greater than 300 GeV (Atwood et al. 2009), which operates in survey mode. The data were analyzed with the *Fermi* Science Tools package version v9r27p1 available from the *Fermi* Science Support Center (FSSC)⁴. For this analysis, only events belonging to the Pass7 Source class and located in a circular region of interest of 10° radius of 2FGL J2001.1+4352 were selected. Moreover, events with zenith angles greater than 100° were removed to reduce the contamination from the Earth-limb gamma-rays, which are produced by cosmic rays interacting with the upper atmosphere, and time intervals during which the rocking angle of the spacecraft exceeded 52° were excluded. The background model used to extract the gamma-ray signal includes a Galactic diffuse emission component and isotropic components (including residual cosmic rays), which were modeled using the files gal_2yearp7v6_v0.fits and isotropic_iso_p7v6source.txt that are publicly available⁵. The normalizations of the components comprising the total background model were allowed to vary freely during the spectral point fitting. The spectral fluxes were derived with the post-launch instruments response functions P7_V6_SOURCE and by applying an unbinned maximum likelihood technique (Mattox et al. 1996) to events in the energy range spanning 300 MeV to 300 GeV. All the sources from the 2FGL catalog located within 10° radius were included in the model of the region. The source position and initial spectrum parameters in the XML file were set to those of the 2FGL catalog. Flux upper limits at 95% confidence level were computed for those time intervals with a test statistic (TS; Mattox et al. 1996) value below four. The systematic uncertainty in the flux is dominated by the systematic uncertainty in the effective area, which is estimated as 10% at 100 MeV, is increased to 5% at 560 MeV, and is increased to 10% at 10 GeV (Ackermann et al. 2012). The systematic uncertainties are smaller than the statistical uncertainties of the data points in the light curve and spectra.

3.1.2. *Swift*

Swift is equipped with three telescopes: the Burst Alert Telescope (BAT; Barthelmy et al. 2005), which covers the 15 – 150 keV range, the X-ray telescope (XRT; Burrows et al. 2005), which covers the 0.3 – 10 keV energy range, and the Ultra-Violet/Optical telescope (UVOT; Roming et al. 2005), which covering the 180 – 600 nm wavelength range with six bandpass filters.

The results reported here relate to measurements performed with XRT and UVOT. The BAT instrument is not sufficiently sensitive to detect this object: MAGIC J2001+439 is in neither the 70-month BAT catalog (Baumgartner et al. 2013) nor the BAT transient monitor paper (Krimm et al. 2013).

The *Swift* satellite observed the source 15 times in 2010. All XRT observations were carried out using the Photon Counting (PC) readout mode. The dataset was first processed with the XRTDAS software package (v.2.9.3) developed at the ASI Science Data Center (ASDC) and distributed by HEASARC within the HEASoft package (v. 6.15.1). Event files were calibrated and cleaned with standard filtering criteria with the *xrtpipeline* task using the calibration files available in the *Swift* CALDB version 20140120. The average spectra were extracted from the cleaned event files. Events for the spectral analysis were selected within a circle of 20 pixel ($\sim 46''$) radius, which encloses about 90% of the point-spread function (PSF), centered on the source position. The background was extracted from a nearby circular region of 40 pixel radius. Two observations were excluded from the analysis due the very short exposure leading to insufficient number of counts. The ancillary response files (ARFs) were generated with the *xrtmkarf* task applying corrections for PSF losses and CCD defects using the cumulative exposure map. Before the spectral fitting, the 0.3 – 10 keV source energy spectra were binned to ensure a minimum of 20 counts per bin. The results from the *Swift*-XRT observations during the MWL campaign in 2010 are summarized in Table A1. The X-ray count rates and hardness ratios for the intra-night light curve from July 16 (the day with the VHE flare) were extracted from the automatic *Swift* XRT analysis for *Fermi*-LAT sources⁶.

The *Swift*-UVOT observations on MG4 J200112+4352 were conducted with UV filters only (namely W1, M2, and W2). We performed an aperture photometry analysis for all filters in all the observations using the standard UVOT software distributed within the HEASoft 6.13 package and the calibration included in the version 20140120 of the *Swift* CALDB. Counts were first extracted from an aperture of $5''$ radius for all filters and converted to fluxes using the standard zero points (Poole et al. 2008). We excluded a nearby contaminating star from the aperture (USNO B1.0 1338-0359172, photographic magnitudes $B_2=15.81$, $R_2=14.98$; Monet et al. 2003), which is the only one within the extraction region in our UV images. We also tried the “curve of growth” method, which is included in the official software for apertures with FWHM radii for each filter. We obtained compatible results, except for larger errors using the second method. The fluxes were then de-reddened using $E(B - V) = 0.498$ (Schlegel et al. 1998; Schlafly & Finkbeiner 2011) and with $A_\lambda/E(B - V)$ ratios calculated for UVOT filters using the mean galactic interstellar extinction curve from (Fitzpatrick 1999). The results were also carefully checked for other possible contaminations. No intra-observation variability has been detected taking the nearby star into account. The results of *Swift*-UVOT are summarized in Table A2. The results obtained for the individual observations show a peak in the source’s broadband SED at the M2 frequency with the energy flux for the M2 filter being up to a factor of two larger than for the W1 filter. The energy flux for M2 is up to 50% higher than that for W2. Comparable “narrow features” in the SED, which are not expected in regular synchrotron bumps from leptonic the-

⁴ <http://fermi.gsfc.nasa.gov/ssc>

⁵ <http://fermi.gsfc.nasa.gov/ssc/data/access/lat/BackgroundModels.html>, <http://www.swift.psu.edu/monitoring>

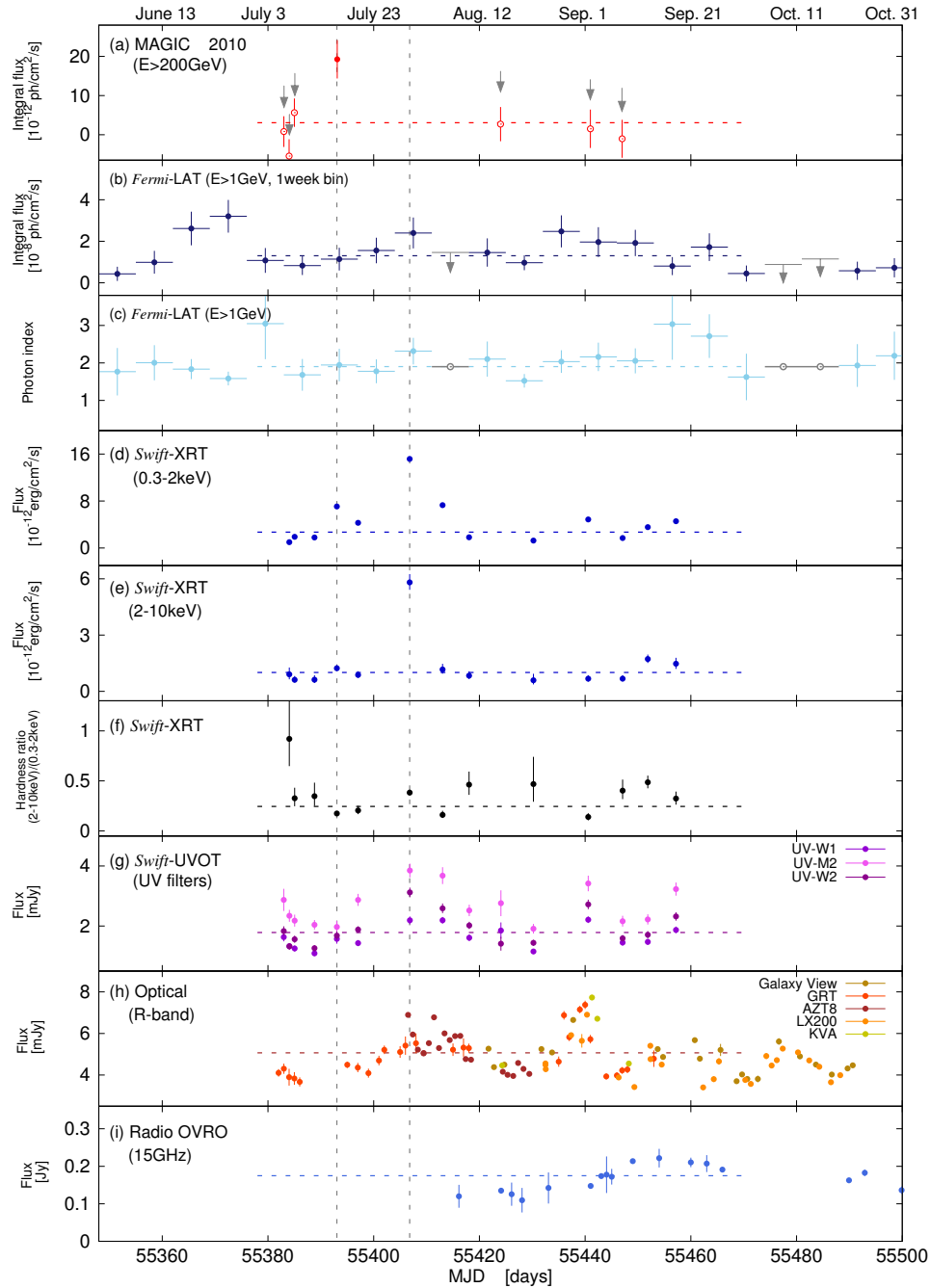


Fig. 3. Multiband light curves of MAGIC J2001+439 during the observing campaign in 2010. All light curves show fluxes from single night observations, except for *Fermi*-LAT. (a) MAGIC light curve above 200 GeV. The red filled circle depicts the flux during the VHE flare on 2010 July 16 (the only significant detection), while the open circles correspond to flux points with excess significances between -1.3 and 1.6σ (calculated according to Li & Ma 1983, Eq.17). The gray arrows report the 95% confidence level upper limits, calculated using a photon index of 2.8. (b) *Fermi*-LAT light curve above 1 GeV with a weekly binning. The gray arrows report the flux upper limits at 95% confidence level, which were calculated (using the photon index of 1.9, reported for this source in the 2FGL catalog) for the time intervals with $TS < 4$. (c) *Fermi*-LAT photon index computed with a weekly binning. The gray open circles denote the assumed photon index for the calculation of the upper limits. (d) *Swift*-XRT light curve in the energy range from 0.3 to 2 keV. (e) *Swift*-XRT light curve in the energy range from 2 to 10 keV. (f) Hardness ratio (2-10 keV) / (0.3-2 keV). (g) *Swift*-UVOT light curves for the three UV filters. (h) Optical R-band light curves from different telescopes (see legend). (i) Radio light curve at 15 GHz from the OVRO telescope. The horizontal dotted lines show the result of a fit with a constant function (the UV-W2 flux points were used for the *Swift*-UVOT light curve). The first and second gray vertical dashed lines denote July 16 and July 29 respectively.

oretical scenarios (see Figures 13, 14, and 15) are observed in the *Swift*-UVOT results for other sources (e.g. see Figure 4 in Archambault et al. 2014), hence we conclude that it is an instrumental effect (not related to the object we are studying). This effect could be due to the source having a $B-V$ that is out of the validity range indicated by Poole et al. (2008) for their flux calibrations in the UV bands. This instrumental effect, however, does not have any impact on the main results reported here.

3.1.3. Optical band

The optical R-band flux density was monitored during the campaign by several instruments. These optical aperture photometry observations were performed with the 35 cm optical telescope at the KVA observatory on La Palma (that operates in close collaboration with the MAGIC telescopes), the Goddard Robotic Telescope (GRT) at the Goddard Geophysical and Astronomi-

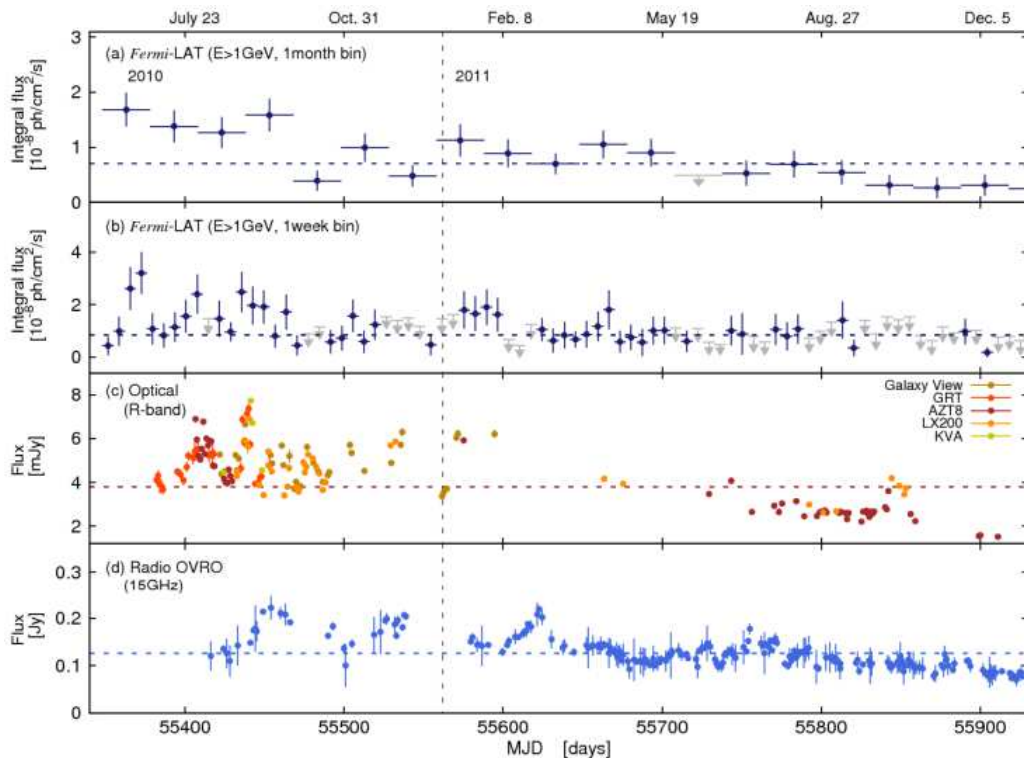


Fig. 4. Long-term light curves of MAGIC J2001+439 in 2010 and 2011. (a) *Fermi*-LAT light curve above 1 GeV with a monthly binning. (b) *Fermi*-LAT light curve above 1 GeV with a weekly binning. The gray arrows report the flux upper limits at 95% confidence level, which were calculated for the time intervals with $TS < 4$. (c) Optical R-band light curves. (d) Radio light curve at 15 GHz. The horizontal dotted lines show the result of a fit with a constant function. See caption of Figure 3 for further details.

cal observatory, the Galaxy View observatory, a 70 cm AZT-8 telescope at the Crimean Astrophysical observatory, and a 40 cm LX-200 telescope in St. Petersburg observatory. All the observed R-band magnitudes were corrected with the Galactic extinction of $A_{\lambda} = 1.219$ mag (Schlafly & Finkbeiner 2011), but the optical data points shown in Figure 3 are not host-galaxy corrected. The typical statistical error is ~ 0.03 mag, which is comparable to the systematic error related to these measurements. For the typical fluxes measured during these observations (15.7 mag), the relative statistical error of the flux measurements is $\sim 3\%$.

As reported in section 3.3.2, the contribution from the host galaxy is small in comparison to the blazar emission. The overall host galaxy emission, when corrected for the Galactic extinction, would be ~ 0.5 mJy. However, the contribution of the host galaxy to the measured blazar emission would depend on the details of the optical observations and data reduction. For the particular case of KVA (which used a fixed aperture radius of 4 arcsec for these observations), the host galaxy contribution to the measured blazar fluxes would be ~ 0.3 mJy. Such estimates for the other telescopes were not performed, but one would expect similar values within ~ 0.1 mJy. Therefore, the subtraction of the constant emission from the host galaxy would only shift the fluxes down by $\sim 6\%$ with an additional difference among instruments at the level of $\sim 2\%$. We considered these small offsets not essential for the results reported in this paper.

3.1.4. Radio band

Radio monitoring at 15 GHz was performed with the 40 m telescope at the Owens Valley Radio Observatory (OVRO) through an ongoing blazar monitoring program⁷. Observations of MAGIC J2001+439 commenced on 2010 August 8 and were scheduled approximately twice per week. The observation and calibration procedures are described in detail in Richards et al.

(2011). Flux densities were measured in a 3 GHz wide band centered at 15.0 GHz, using off-axis dual beam optics with azimuth double switching to remove atmospheric and ground interference. The flux density scale is determined from regular observations of 3C 286 by assuming the value of 3.44 Jy at 15.0 GHz (Baars et al. 1977), which leads to about 5% scale uncertainty and is not included in our error bars. Individual uncertainties are estimated from an error model that accounts for non-thermal random errors in addition to the measured scatter during the observation. The error model works well on average but occasionally produces excessively conservative uncertainties, particularly during poor weather. About 2% of the radio data was excluded due to bad weather.

3.2. Results

3.2.1. Overall multiband light curves

This MWL campaign was conducted over 2.5 months in 2010. The overall MWL light curves of MAGIC J2001+439 during the campaign are shown in Figure 3. From all the MAGIC observations, only the one from 2010 July 16 yielded a significant detection. The other observations yielded excesses with a signal significance below 2σ . In the light curve, we show the photon fluxes and also the 95% confidence level flux upper limits calculated night by night during 2010 July to September. The upper limits were derived by assuming a power-law spectrum with a photon index of $\Gamma = 2.8$, which is the one measured for the observation on 2010 July 16. We note that the computed upper limits depend on the assumed photon index. When using a photon index of $\Gamma = 4.0$, the upper limits increase $\sim 5\%$. The integral flux above 200 GeV on 2010 July 16 is $F_{200\text{GeV}} = (1.9 \pm 0.5) \times 10^{-11}$ ph cm⁻² s⁻¹, which corresponds to $\sim 9\%$ the flux of the Crab Nebula. The integral flux upper limit during the non-detection period in 2009 November shows $F_{200\text{GeV}} < 1.0 \times 10^{-11}$ ph cm⁻² s⁻¹ above 200 GeV. The *Fermi*-LAT light curve is plotted with a temporal bin width of one week

⁷ <http://www.astro.caltech.edu/ovroblazars>

in the energy range from 1 to 300 GeV. The one-week averaged *Fermi*-LAT photon index (for a power-law function above 1 GeV) was also computed (see third panel in Figure 3), indicating the absence of spectral variability (on weekly timescales) during the three-month observing campaign.

The multiband light curves from Figure 3 show that MAGIC J2001+439 is variable at all energy bands with the largest flux variations in the X-ray light curve. It is worth noting the 2-10 keV X-ray flux during the VHE flare from July 16 is only twice as large as that measured during previous *Swift*-XRT observations in 2010 July, while the 2-10 keV flux from July 29 (MJD 55406) is ~five times higher than that of July 16. The 0.3-2 keV X-ray light curve shows the same trend as the variation of the 2-10 keV X-ray light curve, and the hardness ratio also changes in this campaign. Unfortunately, bad weather conditions precluded MAGIC observations on July 29. Moreover, the OVRO monitoring observations started soon after the announcement of the first VHE detection (Mariotti et al. 2010).

In Figure 4, we report the long-term light curves at GeV gamma-rays, optical, and radio bands, as a result of a dedicated optical/radio follow-up during more than one year. The emission in these three energy bands shows a gradual decrease from 2010 through 2011. Further details on the long-term variability and correlations are discussed in sections 3.2.3 and 3.2.4.

3.2.2. July 16 intranight light curves

The intranight light curves of MAGIC J2001+439 on 2010 July 16 are shown in Figure 5. The top panel shows the light curve of the MAGIC observations with an interval of 20 minutes in the energy range above 200 GeV. A constant fit to the data yielded a flux above 200 GeV of $F_{200\text{GeV}} = (1.8 \pm 0.5) \times 10^{-11} \text{ ph cm}^{-2} \text{ s}^{-1}$ with a $\chi^2/n_{\text{dof}} = 9.3/4$, which corresponds to a χ^2 probability of $P_\chi = 5.4\%$. This indicates that the MAGIC light curve is consistent with a constant flux hypothesis within 95% confidence level. The *Swift*-XRT intranight light curve and the hardness ratio plots are shown in the same figure, respectively. The fit with a constant to the X-ray count rate gives a χ^2 of 12.3 for $n_{\text{dof}} = 11$ ($P_\chi = 34\%$), and to the hardness ratio curve gives a χ^2 of 2.9 for $n_{\text{dof}} = 2$ ($P_\chi = 23\%$). We did not detect any statistically significant intra-night variability.

3.2.3. Fractional variability

To quantify the energy dependence of variability amplitudes, we computed the fractional variability amplitude of the light curves for each spectral band (Vaughan et al. 2003). The fractional variability amplitude F_{var} is calculated as

$$F_{\text{var}} = \sqrt{\frac{S^2 - e^2}{F^2}}, \quad (2)$$

where S^2 is the total variance of the light curve, e^2 is the mean squared error, F is the mean flux.

The uncertainty of F_{var} is defined as

$$\Delta F_{\text{var}} = \sqrt{F_{\text{var}}^2 + \text{err}(\sigma_{\text{NXS}}^2)} - F_{\text{var}}, \quad (3)$$

as reported in Poutanen et al. (2008).

The $\text{err}(\sigma_{\text{NXS}}^2)$, which is the error in the normalised excess (NXS) variance, is given by equation 11 of Vaughan et al. (2003)

$$\text{err}(\sigma_{\text{NXS}}^2) = \sqrt{\left(\sqrt{\frac{2}{N}} \frac{e^2}{F^2}\right)^2 + \left(\sqrt{\frac{e^2}{N}} \frac{2F_{\text{var}}}{F}\right)^2}. \quad (4)$$

This methodology to quantify the variability has some caveats. The fractional variability F_{var} is determined for the temporal bin and the source sampling from the light curves used, and

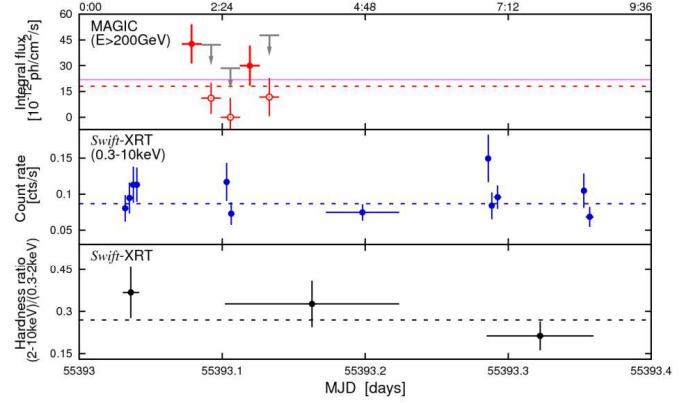


Fig. 5. Intra-night multiband light curves of MAGIC J2001+439 observations on 2010 July 16. Top panel: VHE gamma-ray flux above 200 GeV, as measured by MAGIC. The open circles depict the fluxes with excess significances between 0 and 1.2 σ (calculated according to Li & Ma 1983, Eq. 17). The gray arrows report the 95% confidence level upper limits. The magenta solid line depicts 10% of the Crab Nebula flux, while the red dashed line reports the result of a fit with a constant function ($\chi^2/n_{\text{dof}} = 9.3/4$). Middle panel: X-ray count rate in the energy range 0.3-10 keV, as measured by *Swift* XRT. The blue dashed line depicts the result of a fit with a constant function ($\chi^2/n_{\text{dof}} = 12.3/11$). Bottom panel: Hardness ratio (2-10 keV)/(0.3-2 keV). The black dashed line depicts the result of a fit with a constant function ($\chi^2/n_{\text{dof}} = 2.9/2$). The X-ray count rate and hardness ratios were extracted from the automatic *Swift* XRT analysis for LAT sources⁶

the source variability might actually depend on that. In other words, a densely sampled light curve with very small temporal bins might allow us to see flux variations that are hidden otherwise, and hence we might obtain a larger F_{var} . In the set of light curves shown in Figure 3 and Figure 4, one can see that some energy bands are better sampled than others. In particular, the information from the gamma-ray band is limited with only seven observations performed with MAGIC and fluxes on weekly/monthly time intervals (instead of daily time intervals) obtained with *Fermi*-LAT. Another caveat is that the fractional variability given by equation (2) expects data points with similar error bars (within one dataset). A few data points with substantially (by factors of a few) larger error bars would have a larger impact in e^2 than in S^2 , hence biasing F_{var} towards lower values. In our multi-instrument dataset, the band that is most affected by this effect is the 15 GHz radio light curve provided by OVRO. Despite the above-mentioned caveats, the F_{var} from Vaughan et al. (2003) is a useful methodology to quantify in a simple way the variability in the different energy bands sampled during this observing MWL campaign.

Figure 6 shows the fractional variability obtained with the data reported in the light curves from Figure 3 and Figure 4. The obtained F_{var} values for all energy bands are listed in Table 1. During the MWL campaign in summer 2010, we measured significant F_{var} values for the optical, UV, X-ray, and VHE gamma-ray bands with the variability being greatest at X-ray and VHE. The F_{var} at VHE is dominated by the large flux increase during the flaring activity on July 16, although this F_{var} value needs to be taken with caveats due to the small number of observations in comparison with those performed at other energy bands and the lack of VHE observations during the strong X-ray flare on July 29. As for the long-term behavior, we measure significant F_{var} values in the three bands sampled, namely radio, optical and HE gamma-rays. The fractional variability obtained for these three bands is similar.

3.2.4. Multiband correlations

We quantified the correlation among the MWL light curves shown in Figure 3 and Figure 4 by applying the Discrete Corre-

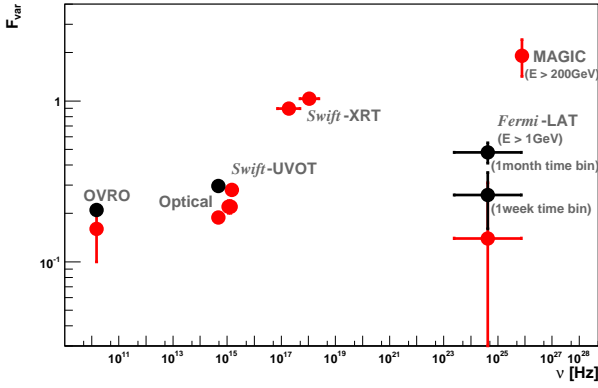


Fig. 6. Fractional variability vs. energy. The red data points refer to the MWL campaign light curves in 2010 July to September reported in Figure 3, while the black data points refer to the long-term light curves in 2010 to 2011 reported in Figure 4.

Table 1. Fractional variability amplitudes for different energy bands and two time periods.

Energy bands	$F_{var} \pm \Delta F_{var}$
(campaign in 2010)	
MAGIC ($E > 200$ GeV)	1.92 ± 0.50
Fermi-LAT one-week bins ($E > 1$ GeV)	0.14 ± 0.17
Swift-XRT (2 – 10 keV)	1.03 ± 0.05
Swift-XRT (0.3 – 2 keV)	0.90 ± 0.01
Swift-UVOT (W2)	0.28 ± 0.02
Swift-UVOT (M2)	0.22 ± 0.02
Swift-UVOT (W1)	0.22 ± 0.02
Optical (R-band)	0.19 ± 0.01
Radio (15 GHz)	0.16 ± 0.06
(long-term in 2010 – 2011)	
Fermi-LAT one-month bins ($E > 1$ GeV)	0.48 ± 0.07
Fermi-LAT one-week bins ($E > 1$ GeV)	0.26 ± 0.10
Optical (R-band)	0.30 ± 0.01
Radio (15 GHz)	0.21 ± 0.01

lation Function (DCF) technique from Edelson & Krolik (1988) to investigate the correlation between different energy bands for different time lags. For each of these pairs, we can compute the unbinned discrete correlation functions (UDCF),

$$UDCF_{ij} = \frac{(F_{a_i} - F_a)(F_{b_j} - F_b)}{\sqrt{(S_a^2 - e_a^2)(S_b^2 - e_b^2)}}, \quad (5)$$

where F_{a_i} and F_{b_j} are the data pair in the bin associated with the pairwise time lag $\Delta t_{ij} = t_j - t_i$, F_a and F_b are the mean flux values, S_a and S_b are the standard deviations, and e_a^2 and e_b^2 are the mean measurement errors squared, respectively.

The DCF for a given time lag of τ is then constructed as

$$DCF(\tau) = \frac{1}{M} \sum_{ij} UDCF_{ij}(\Delta t_{ij}), \quad (6)$$

where the sum runs over the M pairs of observations separated by $\tau - \Delta\tau/2 \leq \Delta t_{ij} \leq \tau + \Delta\tau/2$, where $\Delta\tau$ is the chosen bin width. The uncertainty on the value of the DCF in a given bin is calculated as the RMS variance of all the contributing $UDCF_{ij}$ about the value $DCF(\tau)$,

$$\sigma_{DCF}(\tau) = \frac{1}{M-1} \left(\sum [UDCF_{ij} - DCF(\tau)]^2 \right)^{\frac{1}{2}}. \quad (7)$$

We investigated the correlation among the different bands shown in Figure 3, obtaining a significant correlation only for the UV vs. optical band. Figure 7 shows that the DCF for time lags of ± 30 days for the UV (W2) and optical (R) band. We used 5-day bins for the time lags, which minimizes the impact of the 2–3 day time gaps in the UV data. The plots show clearly that the significant correlation occurs only for a time lag zero. The Pearson’s correlation coefficient⁸ for these two datasets (depicted in the right panel in Figure 7) is $r = 0.90$ with an accidental probability P of no-correlation⁸ of 0.04% (with $n_{\text{dof}} = 8$). The significant correlation is not surprising, given the proximity of these two energy bands.

The DCF plots for long-term light curves from Figure 4 are reported in Figure 8. The three panels show an overall positive correlation for all time lags, which is produced by the clear long-term decrease in the radio/optical/gamma-ray fluxes over many month timescales. The DCF for *Fermi* vs. radio and *Fermi* vs. optical cover ± 0.5 years with 30-day time lag bins. The large error bars in the DCF values, which are caused by the relatively large error bars in the gamma-ray fluxes, preclude the investigation of any temporal structure in the correlation.

The DCF for the optical vs. radio flux cover time lags from -50 days to +120 days with a temporal bin of 5 days. The asymmetry is driven by the result that the radio observations started about one month after the optical observations, and they extend further in time than the optical observations. This means that there is a lower tolerance to apply negative time shifts (i.e. the optical light curve is shifted to earlier times) and a higher tolerance to apply positive time shifts (i.e. the optical light curve is shifted to later times). Given the large number of data points and the relatively small single-night measurement errors, the errors in the DCF values are small, which indicates a temporal structure on the top of the overall positive correlation. The DCF is highest in the time lag range from 0 to +50 days with a maximum value at about +40 days. To investigate this DCF peak at about 40 days, we computed the normalized optical and radio long-term light curves, where the data flux values of each measurement are divided by the mean flux of the entire light curve. There are some structures in the optical and radio light curves that are similar in amplitude and are better aligned when shifting the optical light curve by +40 days; yet, there are also several other structures, which occur in one band and not in the other. Moreover, we note that +40 days is the minimum time lag needed to get the optical light curve starting at the same day as the radio light curve. Given the different length and density of observations for these two bands, we cannot make definite conclusions about the temporal structure observed in the DCF for these two bands, apart from the positive correlation produced by the long-term decrease in the light curves. Further studies would require more homogeneous and better sampled light curves.

Figure 9 shows flux-flux linear correlation plots of time lag zero for long-term light curves. The derived Pearson’s correlation coefficients are $r = 0.59$ for the GeV gamma-ray vs. optical R-band, $r = 0.43$ for the GeV gamma-ray vs. radio, and $r = 0.48$ for the radio vs. the optical R-band. The accidental probabilities are $P = 2.0\%$ (with number of degrees of freedom $n_{\text{dof}} = 13$), $P = 10.0\%$ (with $n_{\text{dof}} = 14$), and $P = 0.3\%$ (with $n_{\text{dof}} = 35$) for GeV/optical, GeV/radio and radio/optical, respectively. These values indicate that there is a marginally significant positive linear correlation among the GeV/optical bands, and a much more significant positive correlation for the radio/optical bands. The higher significance for the correlation between the radio/optical bands is due to the larger number of measurements and smaller uncertainties in the measured fluxes (as implied by formulae 5, 6, and 7).

⁸ This is a standard formulation that one can find in section 14.5 of Press et al. (1992).

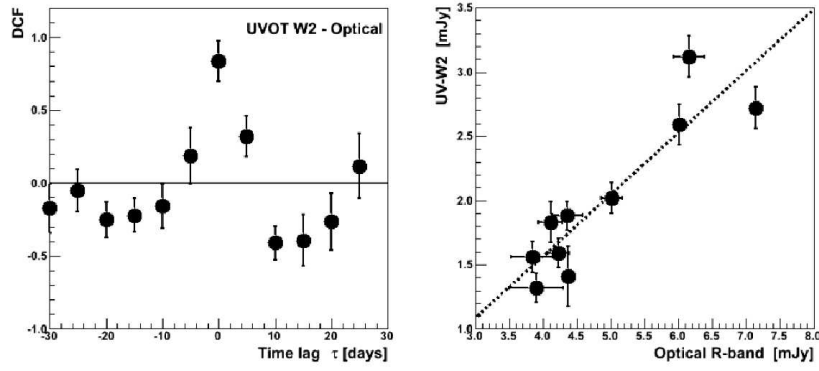


Fig. 7. Discrete correlation function for different time lags computed for the UV (W2) and optical (R) data obtained during the MWL campaign in 2010 and the flux linear correlation plot for a time lag of zero. The dotted line shows the best fit with a linear function.

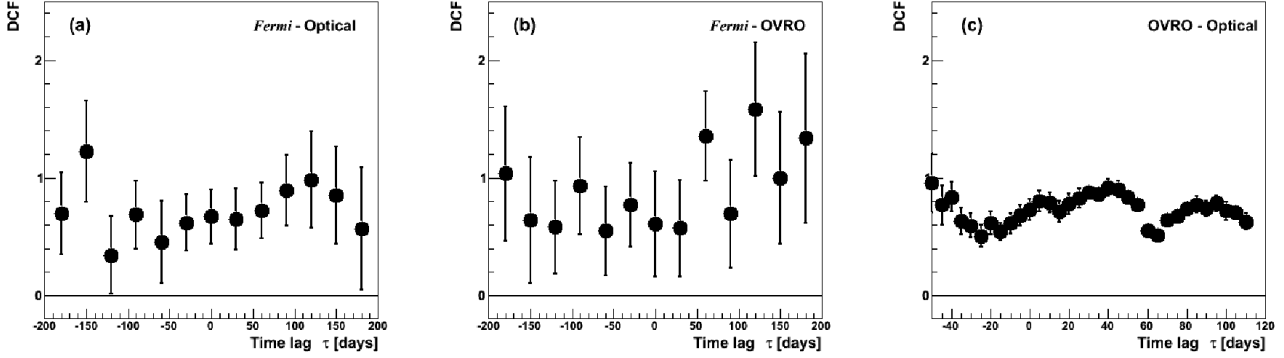


Fig. 8. Discrete correlation function for different time lags for the long-term light curves from Figure 4. (a) One-month-averaged *Fermi*-LAT fluxes ($E > 1$ GeV) vs. one-month-averaged optical R-band fluxes. (b) One-month-averaged *Fermi*-LAT fluxes ($E > 1$ GeV) vs. one-month-averaged radio 15 GHz fluxes. (c) Radio 15 GHz fluxes vs. optical R-band fluxes (only single observations occurring during the same day were used).

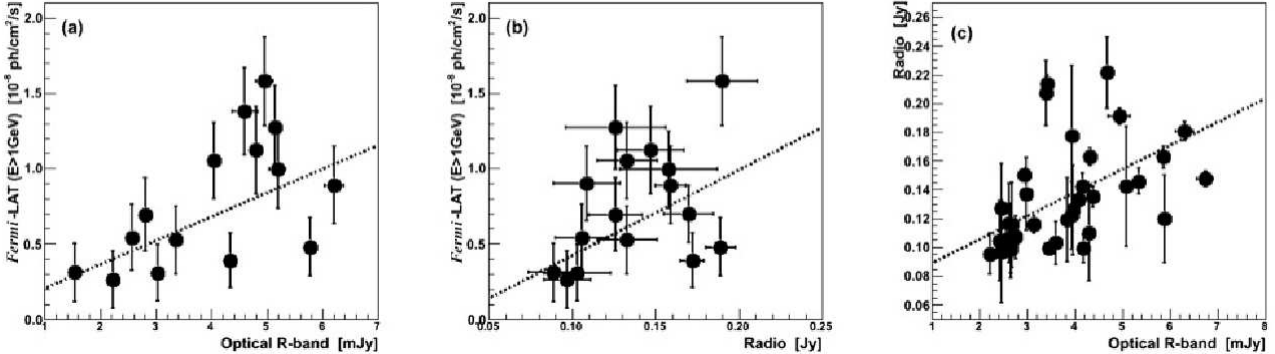


Fig. 9. Flux-flux linear correlation plots for a time lag of zero for the long-term light curves reported in Figure 4. (a) One-month-averaged *Fermi*-LAT fluxes ($E > 1$ GeV) vs. one-month-averaged optical R-band fluxes. (b) One-month-averaged *Fermi*-LAT fluxes ($E > 1$ GeV) vs. one-month-averaged radio 15 GHz fluxes. (c) Radio 15 GHz fluxes vs. optical R-band fluxes. (Only single observations occurring during the same day were used.) The dotted line shows the best fit with a linear function.

3.3. Redshift measurement of the blazar MAGIC J2001+439

Since the redshift of MAGIC J2001+439 was still uncertain, we used two independent methods to determine it.

3.3.1. Redshift estimation using the gamma-ray spectrum

The redshift of a gamma-ray source can be estimated (or at least constrained) using the measured gamma-ray spectra, once a particular EBL model is assumed. In this work, we adopted the EBL model from Franceschini et al. (2008). If we assume that the intrinsic source gamma-ray spectrum can be expressed by a simple power-law function $dN/dE \propto E^{-\Gamma_{\text{int}}}$, where the fitted intrinsic photon index is Γ_{int} , one can set upper limits on the source redshift under the assumption that the intrinsic source gamma-ray spectrum cannot be harder than 1.5. This limit is physically

motivated from shock acceleration arguments, as discussed in Aharonian et al. (2006). As shown in Figure 10, when taking the uncertainty in the measured VHE spectrum with MAGIC into account, we find that this assumption yields an upper limit on the redshift of $z < 0.6$ with a 95% confidence level.

Another estimate on the redshift can be obtained using the measured gamma-ray spectra with *Fermi* and MAGIC, as reported in Prandini et al. (2011). We analyzed *Fermi*-LAT data from MAGIC J2001+439 between 2010 July 1 and August 1 and obtained a one-month-averaged *Fermi*-LAT spectrum. This spectrum has a spectral index of $\Gamma_{\text{LAT}} = 1.83 \pm 0.18$, when being characterized by a power-law function in the energy range between 300 MeV and 30 GeV. The integral flux is $F_{300\text{MeV}} = (3.9 \pm 0.8) \times 10^{-8} \text{ ph cm}^{-2} \text{ s}^{-1}$ in the energy range above 300 MeV. We define the redshift of z^* by requiring that the power-

law index of the observed VHE gamma-ray spectrum, when corrected for the EBL absorption, is equal to the power-law index of $\Gamma = 1.83$ observed by *Fermi*-LAT at energies which are not affected by the EBL absorption. As shown in Figure 10, this procedure leads to $z^* = 0.31 \pm 0.16$. In this calculation, we did not consider instrumental systematic errors in the determination of the spectral indices from MAGIC and *Fermi*-LAT. We followed the prescription given in Prandini et al. (2011) with the difference that, we also considered the uncertainty in the power-law index from the HE spectrum measured with *Fermi*, in addition to the uncertainty in the power-law index from the VHE spectrum when computing the uncertainty in the parameter z^* . Therefore, our uncertainty in the parameter z^* is larger, but more reliable than the one that would have been derived following Prandini et al. (2011). To determine the reconstructed redshift z_{rec} , we used the empirical relation reported in Prandini et al. (2011) that relates the true redshifts of known distance sources z_{true} with their z^* values, $z^* = A + Bz_{\text{true}}$, where $A = 0.036 \pm 0.014$ and $B = 1.60 \pm 0.14$. Using this prescription, we obtain a reconstructed redshift $z_{\text{rec}} = 0.17 \pm 0.10$. The systematic uncertainty related to this method is estimated to be 0.05 in the redshift value.

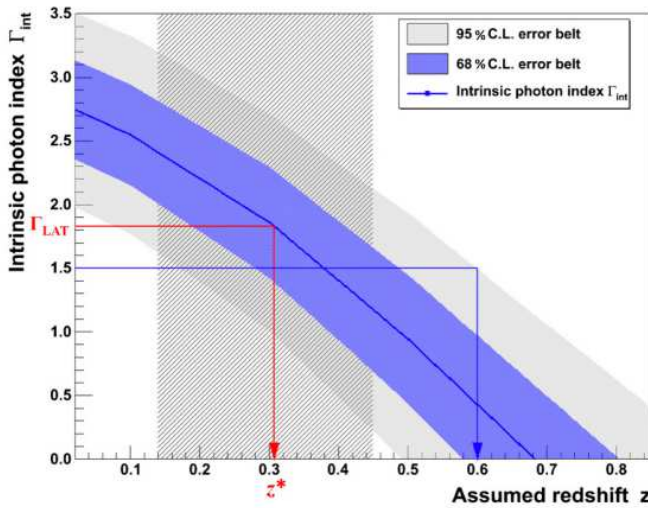


Fig. 10. Intrinsic photon index Γ_{int} as a function of the redshift assuming the EBL model from Franceschini et al. (2008). The blue and gray filled areas correspond to the 1σ (68%) and 2σ (95%) confidence error belts, respectively. The red arrow indicates the estimated redshift z^* , which is determined by the redshift value at which $\Gamma_{\text{int}} = \Gamma_{\text{LAT}} = 1.83 \pm 0.18$. The diagonal shaded area shows the error range of z^* , where the error takes both the errors on the MAGIC VHE photon index and the *Fermi*-LAT HE photon index into account. See text for calculation of the reconstructed redshift z_{rec} using the value z^* . The blue arrow indicates the 95% confidence level upper limit on the redshift, which is obtained when $\Gamma_{\text{int}} = 1.5$, within the 2σ (95%) confidence error belt.

3.3.2. Redshift determination using the measured flux of the host galaxy

The MAGIC J2001+439 (MG4 J200112+4352) was observed by the NOT telescope on 2013 June 13 to study the host galaxy. To increase the detection probability, the observations were timed to coincide with an optical low state ($R \sim 16.8$, corresponding to $F \sim 1.8$ mJy) of the target. We obtained nine images, each with 900s exposure time, through the I-band filter using the ALFOSC instrument equipped with a 2048×2048 E2V chip with a gain factor of $0.327 e^-/\text{Analog to Digital Units (ADU)}$, and readout noise of $4.2e^-$. The total field of view of ALFOSC is 6.5×6.5 , and the pixel scale is $0''.19/\text{pixel}$. The transparency of the atmosphere remained constant for all the observations, which allowed for photometric measurements. The images were

bias-subtracted and flat-fielded with twilight flats, after which the fringe pattern was removed using an archival fringe map. Individual images were then registered using 13 stars over the field of view and co-added. The resulting image has a total exposure time of 2h 15min and FWHM of $0''.72$.

The calibration of the field was obtained from I-band observations of MAGIC J2001+439 and BL Lac in photometric conditions with the 72" Perkins Telescope at Lowell Observatory on 2013 November 2 and 3. We first used the BL Lac comparison star sequence in Fiorucci & Tosti (1996) to calibrate five stars in the field of MAGIC J2001+439, and the same stars were then used to calibrate the NOT image. The uncertainty of this calibration is 0.05 mag. As a crosscheck, we performed a second calibration using the N-magnitudes from 25 nearby stars from GSC2.3 and found a difference of $17 \pm 9\%$ between these two calibrations.

To study the host galaxy, we fitted two-dimensional surface brightness models to the observed light distribution of MAGIC J2001+439. Details of this process can be found in Nilsson et al. (1999, 2003). In short, we first determined the background level around MAGIC J2001+439 and a nearby star S1 (Figure 11) by removing the background tilt and then measuring empty sky regions around the targets. Next, we determined the PSF from two field stars located 55 arcsec and 92 arcsec away from MAGIC J2001+439. These fields were carefully selected not to be contaminated by foreground/background stars and roughly equal to MAGIC J2001+439 in peak intensity. The two field stars were close enough to have the same PSF. We then fitted the PSF to MAGIC J2001+439 and S1 and subtracted the resulting model, which accurately removed the star S1 (showing a good fit with the PSF model) but revealed a clear excess around MAGIC J2001+439. The latter was then fitted with a model consisting of an unresolved nucleus and a host galaxy, represented by the Sérsic (1968) profile with Sérsic index $n = 4$ (de Vaucouleurs profile). The number of free parameters in this fit was nine: position and magnitude of the nucleus (x_n, y_n, m_n), host galaxy position (x_g, y_g), magnitude (m_g), effective radius (r_e), ellipticity (ϵ), and position angle (PA), which is defined counter-clockwise from the North. The fit was performed using pixels within 5.7 arcsec from the center of MAGIC J2001+439, excluding any pixels affected by overlapping targets and subtracting S1 prior to the fit.

The results of these fits are summarized in Figures 11 and 12 and Table 2. In addition to the best-fit values, we give the errors of the fitted parameters (σ_{fit}) and the calibration error (σ_{cal}) in Table 2. The former were estimated with ~ 100 Monte Carlo simulations of the fit, which included the effects of photon noise, readout noise background uncertainty, and PSF variability (see Nilsson et al. 2003, for details). We were not able to obtain a perfect fit (reduced $\chi^2 = 3.03$) mainly due to the PSF mismatch in the core of MAGIC J2001+439 and noise in the PSF wings, both of which were not included in the noise model. However, our simulations include these effects and show that the results are not biased in any way due to not achieving a reduced $\chi^2 = 1.0$.

The redshift of MAGIC J2001+439 was estimated using the observed host galaxy magnitude $I = 17.15 \pm 0.06$ and the result by Sbarufatti et al. (2005) that the luminosities of BL Lac host galaxies are confined to a relatively narrow range of $M_R = -22.8 \pm 0.5$. We used $R - I = 0.7$, leading to $M_I = -23.5$, the K-correction from Fukugita et al. (1995), and the evolution correction $E(z) = 0.84 \cdot z$ to iteratively determine the redshift consistent with $I = 17.15$ and $M_I = -23.5$. For the galactic extinction, we used the value in NED, $A_I = 0.846$, which is based on the dust reddening study by Schlafly & Finkbeiner (2011). The redshift was estimated 1000 times with each time drawing I , M_I , and A_I from a Gaussian distribution with standard deviations of 0.06, 0.5, and 0.14, respectively. The resulting z distribution is roughly Gaussian with average $z = 0.18$ and standard deviation

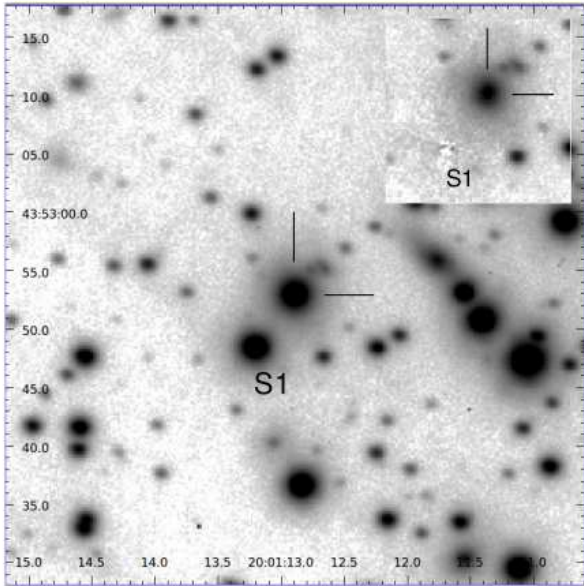


Fig. 11. Portion of the NOT I-band image. Field size is $50'' \times 50''$. North is up, and east is to the left. MAGIC J2001+439 and a nearby star (S1) are indicated. The inset shows MAGIC J2001+439 and S1 after subtracting a properly scaled PSF, showing the host galaxy more clearly.

Table 2. Host galaxy fit results. σ_{fit} gives the statistical error of each parameter as determined by error simulations, and σ_{cal} is the calibration error (see the text for further details).

Parameter	value	σ_{fit}	σ_{cal}
Nucleus magnitude m_n	16.08	0.02	0.05
Host magnitude m_g	17.15	0.04	0.05
Host effective radius r_e	$2''.4$	$0''.4$	
Host ellipticity ϵ	0.15	0.03	
Host PA	178°	3°	

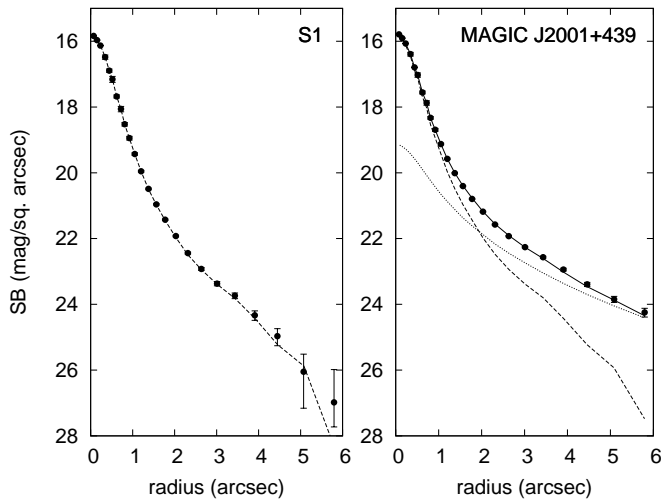


Fig. 12. Surface brightness profiles of star S1 and MAGIC J2001+439 with model profiles: nucleus + host galaxy (solid line), nucleus (dashed), and host galaxy (dotted).

$\sigma_z = 0.04$. It should be noted that almost all uncertainty in this z estimate arises from the relatively broad distribution of M_I .

A potential bias (systematic error) in this estimation could come from the assumption of the true BL Lac host galaxy luminosity distribution. In this respect, Shaw et al. (2013) studied the host galaxies of 475 *Fermi* BL Lacs and obtained an average host galaxy luminosity of $M_R = -22.5$, which is 0.3 mag fainter than the flux $M_R = -22.8 \pm 0.5$ used here (retrieved from

Sbarufatti et al. 2005). If we used $M_R = -22.5$ in our calculation, we would obtain $z = 0.16 \pm 0.04$, which is well within the statistical uncertainties of our measurement. Moreover, it should be stressed that Shaw et al. (2013) reported that their result may be biased because they studied targets, which had no host detections at the time of their study, which means that they were probably selecting targets with fainter hosts (the brighter hosts were already detected by earlier authors).

The two redshift measurements reported in section 3.3.1 and 3.3.2 ($z = 0.17 \pm 0.10$ and $z = 0.18 \pm 0.04$) are compatible and consistent with the rough estimate reported by Bassani et al. (2009), and the lower limit reported by Shaw et al. (2013). The second method (using the optical measurement of the host galaxy) is more reliable because it uses less assumptions and yields a smaller uncertainty in the redshift value. We use $z = 0.18$ throughout the rest of this paper.

4. Discussion

In Figure 13, we show the simultaneous MWL SED of MAGIC J2001+439 on 2010 July 16. The MAGIC data points show the deabsorbed spectrum with a redshift of $z = 0.18$ using the EBL model of Franceschini et al. (2008). The deabsorbed spectrum is compatible with a simple power law with photon index $\Gamma = 2.3 \pm 0.4$. A one-zone SSC model, as described in the appendix of Takami (2011) was used to interpret the MWL SED. In this model, the emission region is assumed to be spherical with radius R and to be filled by a tangled magnetic field of intensity B in a comoving frame. The emission region is in motion with a Lorentz factor of Γ and a viewing angle of θ in the observer frame. The injected energy distribution of the relativistic emitting electrons is described by an unsmoothed broken power-law function⁹,

$$N(\gamma) = \begin{cases} K\gamma^{-n_1} & (\gamma_{\min} < \gamma < \gamma_{\text{bk}}) \\ K\gamma_{\text{bk}}^{n_2-n_1}\gamma^{-n_2} & (\gamma_{\text{bk}} < \gamma < \gamma_{\max}), \end{cases} \quad (8)$$

where K is the normalization factor of the electron density, extending from γ_{\min} to γ_{\max} with indices n_1 and n_2 below and above the break Lorentz factor γ_{bk} , respectively. Relativistic effects are taken into account by the Doppler factor $\delta = [\Gamma(1 - \beta\cos\theta)]^{-1}$. We obtained the following one-zone SSC scenario parameters: $\gamma_{\min} = 1.0$, $\gamma_{\text{bk}} = 3.9 \times 10^4$, $\gamma_{\max} = 6.0 \times 10^5$, $n_1 = 2.0$, $n_2 = 4.8$, $K = 5.2 \times 10^3 \text{ cm}^{-3}$, $B = 55 \text{ mG}$, $R = 20.4 \times 10^{15} \text{ cm}$ and $\delta = 27$, where we used the redshift $z = 0.18$, which is the value derived from the dedicated measurement reported in section 3.3.2. The parameters γ_{\min} and n_1 had been initially set to 1 and 2.0, respectively. The estimated synchrotron emission peak of MAGIC J2001+439 is located at a high frequency $\sim 10^{16} \text{ Hz}$, which indicates that this object is a typical HBL. The simultaneous MWL SED of MAGIC J2001+439 on 2010 July 16 can be described well by a one-zone SSC scenario.

Figure 14 shows the SED of the X-ray flare on 2010 July 29 with the simultaneous data from *Fermi*-LAT, *Swift*-XRT/UVOT, and optical R-band. There are no VHE gamma-ray observations due to bad weather at the MAGIC site. The X-ray spectrum from July 29 with a photon index of 2.5 ± 0.1 seems to be harder than that from July 16, for which we obtained a photon index of 2.9 ± 0.2 . The synchrotron component in the energy band between radio and X-rays shows significant variability (see Figure 3). We also find a simultaneous increase of the UV energy flux during the X-ray flare. Therefore, we tried to parameterize the SED from July 29 by changing few parameters (with respect to the model used for July 16) by describing the electron spectrum, while keeping the environmental parameters constant of the model. The obtained one-zone SSC model parameters that reproduce the observed SED data are summarized in

⁹ The code described in Takami (2011) can parameterize the electron energy distribution with both a smoothed and unsmoothed broken power law.

Table 3. The increase and hardening of the X-ray spectrum is parameterized by an increase in the electron number density (K increased from $5.2 \times 10^3 \text{ cm}^{-3}$ to $7.3 \times 10^3 \text{ cm}^{-3}$) and a hardening in the slope of the electron spectrum above the break energy (n_2 changed from 4.8 to 4.3). This could be interpreted as an injection of fresh relativistic electrons into the emission region, which should also cause a higher flux in the gamma-ray bands. According to this theoretical scenario, both the synchrotron and the SSC bumps went up substantially during this X-ray flare. The observational data can only confirm the large increase in the synchrotron bump. However, we also note that such a change in the SED could have been produced by alternative scenarios, such as a change in the magnetic field strength. More higher quality gamma-ray data would be required to discriminate between different scenarios.

Figure 15 shows the contemporaneous broadband SED for the 2.5 month-long MWL campaign. The figure shows both the MAGIC spectrum energy flux point with a significance (per data point) below 2σ and 95% confidence level upper limits, which were calculated assuming a power-law spectrum with a photon index of $\Gamma = 2.8$. We analyzed the 2.5 months-averaged *Fermi*-LAT spectrum during the MWL campaign in 2010 (which corresponds to the periods of the *Swift* observations). The *Fermi*-LAT spectrum between 300 MeV and 100 GeV can be characterized by a power-law function with a spectral index of $\Gamma_{\text{LAT}} = 2.02 \pm 0.08$. The integral flux above 300 MeV is $F_{300\text{MeV}} = (5.0 \pm 0.6) \times 10^{-8} \text{ ph cm}^{-2} \text{ s}^{-1}$. To describe the measured SED with the one-zone SSC model, we had to lower the value of γ_{bk} with respect to the one used to describe the SED from July 16. Within this theoretical scenario, this indicates that, the energy distribution of relativistic electrons extended to higher energies in July 16, when the VHE gamma-ray flare was detected with MAGIC.

5. Conclusions

We performed a detailed study of the broadband emission of 2FGL J2001.1+4352 (previously named OFGL J2001.0+4352), which had been associated to the bright radio source MG4 J200112+4352 in Bassani et al. (2009) and identified as a promising VHE emitter by the *Fermi*-LAT collaboration in 2009 October. We characterized the radio to VHE SED and quantified the multiband variability and correlations over short (few days) and long (many months) timescales.

The planned MAGIC observations led to the first VHE detection of this object, which we named MAGIC J2001+439. The multi-instrument observations showed variability in all the energy bands with the highest amplitude of variability in the X-ray and VHE bands. This source was significantly detected at VHE only during a 1.3 hour long MAGIC observation on 2010 July 16. The time-averaged VHE spectrum during this night can be described by a power-law function from 78 GeV to 500 GeV with a differential photon index $\Gamma = 2.8 \pm 0.4$ and a flux normalization at 200 GeV $f_0 = (1.9 \pm 0.4) \times 10^{-10} \text{ cm}^{-2} \text{ s}^{-1} \text{ TeV}^{-1}$, which gives about 9% the flux of the Crab Nebula above 200 GeV. During the other nights, the VHE flux was lower than 5% the Crab Nebula flux. Besides the variability on few-day timescales, the long-term monitoring of MAGIC J2001+439 showed that the gamma-ray, optical, and radio emission gradually decreased on few-month timescales from 2010 through 2011, indicating that the overall radio, optical, and gamma-ray emission is produced (at least a fraction of it) in a single region by the same population of particles. A similar positively correlated trend in the GeV/optical and the radio/optical bands has been observed on other blazars monitored over many years (e.g. Aleksić et al. 2014a,b).

For the first time, we also determined, the redshift of this BL Lac object through the measurement of its host galaxy

during low blazar activity. Because the luminosities of BL Lac host galaxies are confined to a relatively narrow range (Sbarufatti et al. 2005), we obtained $z = 0.18 \pm 0.04$. Moreover, we used the *Fermi*-LAT and MAGIC gamma-ray spectra to provide an independent redshift estimation (Prandini et al. 2011) by obtaining $z = 0.17 \pm 0.10$. The redshift values computed with these two independent methods are compatible within the quoted errors. The first method is more reliable because it uses fewer assumptions and yields a smaller uncertainty in the redshift value.

We studied the radio-to-VHE SEDs for three periods: 2010 July 16 when the source was significantly detected at VHE with MAGIC; 2010 July 29 when a large X-ray flux was measured (with no simultaneous VHE observations), and the entire dataset from the MWL campaign in summer 2010 with the exclusion of the observations from July 16 and July 29. Using our redshift measurement of $z = 0.18$, we described the three broadband SEDs with a one-zone SSC model. The model parameters that we used are at the boundary of the SSC parameter distribution derived for a TeV blazar sample by Tavecchio et al. (2010). Within this theoretical scenario, we explain the changes in the broadband SEDs observed during the flaring activity in July 16 as produced by an extension of the electron energy distribution towards higher energies (increase in the parameter γ_{bk}) and in the SED observed during the large X-ray flare on July 29 as produced by an increase in the number of electrons (increase in the parameter K) and a hardening of the high-energy tail of the electron energy distribution (hardening of the parameter n_2).

This new VHE detection adds one more BL Lac object, MAGIC J2001+439, to the short list of extragalactic VHE sources¹. Moreover, the redshift measurements we performed determined that this is a relatively distant VHE BL Lac object. The characterization of the broadband SED with simultaneous observations during various activity levels is relevant in understanding the physical properties of the various blazar types and in finally moving towards AGN unification schemes.

Acknowledgements. We would like to thank the anonymous referee for providing detailed and constructive remarks that helped us to improve the manuscript.

We would like to thank the Instituto de Astrofísica de Canarias for the excellent working conditions at the Observatorio del Roque de los Muchachos in La Palma. The support of the German BMBF and MPG, the Italian INFN, the Swiss National Fund SNF, and the Spanish MICINN is gratefully acknowledged. This work was also supported by the CPAN CSD2007-00042 and MultiDark CSD2009-00064 projects of the Spanish Consolider-Ingenio 2010 program, by grant 127740 of the Academy of Finland, by the DFG Cluster of Excellence "Origin and Structure of the Universe", by the DFG Collaborative Research Centers SFB823/C4 and SFB876/C3, and by the Polish MNiSzW grant 745/N-HESS-MAGIC/2010/0.

The *Fermi*-LAT Collaboration acknowledges support from a number of agencies and institutes for both development and the operation of the LAT as well as scientific data analysis. These include NASA and DOE in the United States, CEA/Irfu and IN2P3/CNRS in France, ASI and INFN in Italy, MEXT, KEK, and JAXA in Japan, and the K. A. Wallenberg Foundation, the Swedish Research Council and the National Space Board in Sweden. Additional support from INAF in Italy and CNES in France for science analysis during the operations phase is also gratefully acknowledged.

We gratefully acknowledge the entire *Swift* team, the duty scientists and science planners for the dedicated support, making these observations possible. The data on this paper are based partly on observations made with the Nordic Optical Telescope, operated by the Nordic Optical Telescope Scientific Association at the Observatorio del Roque de los Muchachos, La Palma, Spain, of the Instituto de Astrofísica de Canarias. Part of the data were obtained with ALFOSC, which is provided by the Instituto de Astrofísica de Andalucía (IAA) under a joint agreement with the University of Copenhagen and NOTSA. The St. Petersburg University team acknowledges support from the Russian RFBR foundation, grant 12-02-00452. The authors thank Svetlana Jorstad for kindly providing the optical calibration images.

The OVRO 40 m monitoring program is supported in part by NSF grants AST-0808050 and AST-1109911 and NASA grants NNX08AW31G and NNX11AO43G. TH was supported by the Jenny and Antti Wihuri foundation. The National Radio Astronomy Observatory is a facility of the National Science Foundation operated under cooperative agreement by Associated Universities, Inc.

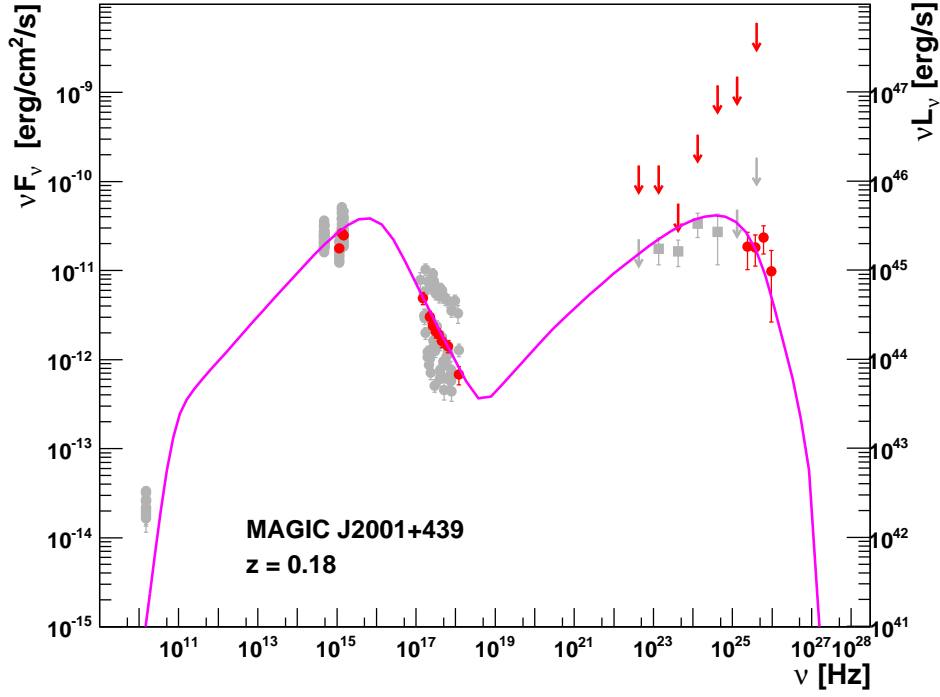


Fig. 13. Broadband SED for 2010 July 16. The simultaneous data are depicted with red filled circles (which involve observations from MAGIC, *Fermi*-LAT, *Swift*-XRT, and *Swift*-UVOT). The gamma-ray data points were corrected for attenuation on the EBL using a redshift $z = 0.18$ and the model from Franceschini et al. (2008). The red arrows show the 95% upper limits for a one-day-averaged *Fermi*-LAT spectrum (MJD: 55392.5 – 55393.5), which is coincident with the MAGIC VHE observation from July 16. The gray filled squares represent the one-month-averaged *Fermi*-LAT spectrum in 2010 July (MJD: 55378 – 55409), and the gray filled circles show all the radio/optical/UV/X-ray data taken during the MWL campaign in 2010, excluding July 16. The magenta solid curve represents the resulting intrinsic spectrum parameterized with a one-zone SSC model. See text for further details.

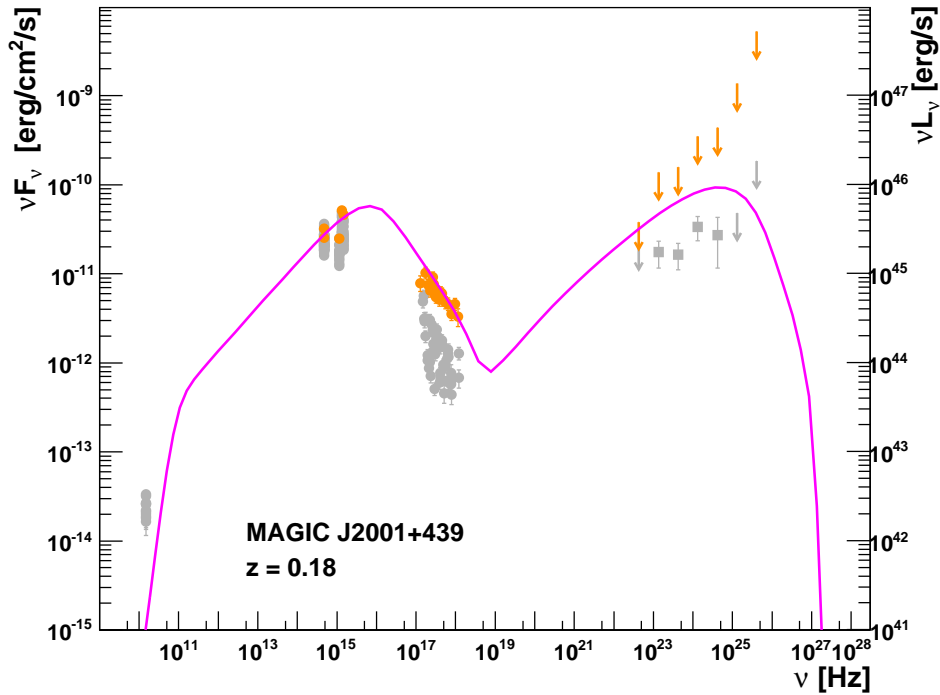


Fig. 14. Broadband SED for 2010 July 29. The simultaneous data are depicted with orange filled circles (which involve observations from *Fermi*-LAT, *Swift*-XRT, *Swift*-UVOT and optical R-band). The gamma-ray data points were corrected for attenuation on the EBL using a redshift $z = 0.18$ and the model from Franceschini et al. (2008). The orange arrows show the 95% upper limits for a one-day-averaged *Fermi*-LAT spectrum (MJD: 55406 – 55407) coincident with the *Swift* observations from July 29. The gray filled squares represent the one-month-averaged *Fermi*-LAT spectrum in 2010 July (MJD: 55378 – 55409), and the gray filled circles show all the radio/optical/UV/X-ray data taken during the MWL campaign in 2010, excluding July 29. The magenta solid curve represents the resulting intrinsic spectrum parameterized with a one-zone SSC model. See text for further details.

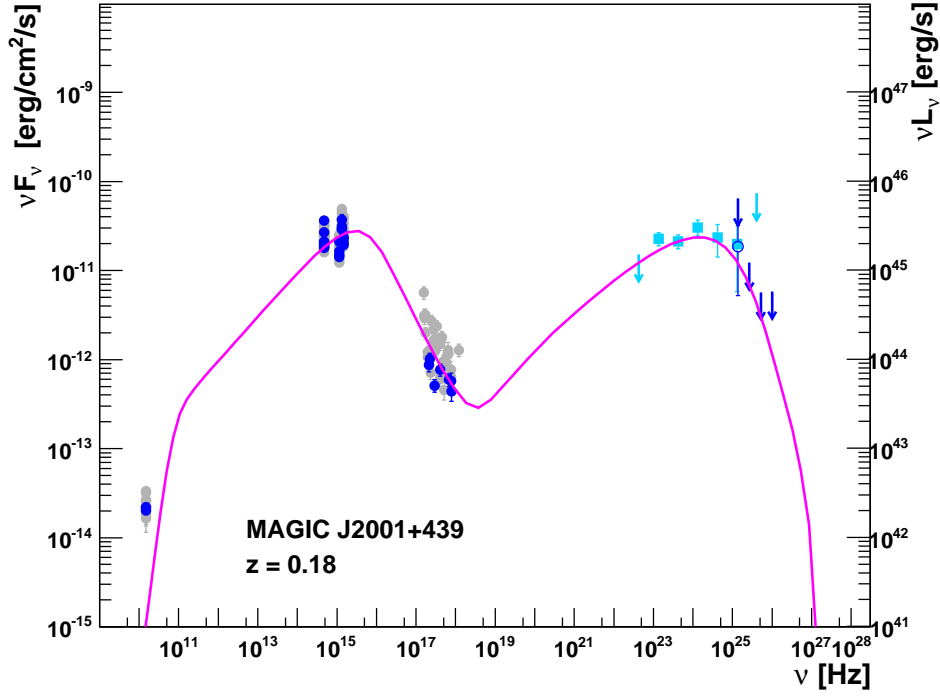


Fig. 15. Contemporaneous broadband SED for the low state during the MWL campaign in 2010. The blue open circle depicts the energy flux computed using all the MAGIC observations during the MWL campaign in 2010, after excluding the data during the VHE flare from 2010 July 16. This MAGIC data point contains a gamma-ray excess with a signal significance (calculated using Eq.17 of Li & Ma 1983) of 1.4σ . The blue arrows report the 95% confidence level energy flux upper limits derived from the MAGIC observations. The cyan filled squares represent the averaged *Fermi*-LAT spectrum from the MWL campaign in 2010 (MJD: 55382 – 55458). The cyan arrows report the *Fermi*-LAT 95% confidence level energy flux upper limits for the energy bins with TS < 4. The gamma-ray data points and upper limits were corrected for attenuation on the EBL using a redshift $z = 0.18$ and the model from Franceschini et al. (2008). The blue filled circles show the *Swift*-XRT, *Swift*-UVOT, optical, and radio data obtained during the days when MAGIC observed the source (with the exception of July 16). The gray filled circles show all the radio/optical/UV/X-ray data taken during the MWL campaign in 2010, excluding July 16 and July 29. The magenta solid curve represents the resulting intrinsic spectrum parameterized with a one-zone SSC model. See text for further details.

Table 3. One-zone SSC model parameters for the three different SEDs reported in Figures 13, 14, and 15.

state	γ_{\min}	γ_{bk} [10^4]	γ_{\max} [10^5]	n_1	n_2	K [10^3 cm^{-3}]	B [mG]	R [10^{15} cm]	δ	z
July 16 (VHE flare detection)	1.0	3.9	6.0	2.0	4.8	5.2	55	20.4	27	0.18
July 29 (X-ray flare)	1.0	3.9	6.0	2.0	4.3	7.3	55	20.4	27	0.18
Typical emission during the campaign	1.0	2.8	6.0	2.0	4.8	5.2	55	20.4	27	0.18

Special thanks to Richard Schwartz, who performed observations with the Galaxy View observatory and diligently reduced the data while fighting against a pancreatic cancer during the last months of his life.

References

- Abdo, A. A., Ackermann, M., Ajello, M., et al., 2009, *ApJS*, 183, 46
- Ackermann, M., Ajello, M., Albert, A., et al., 2012, *ApJS*, 203, 4
- Ackermann, M., Ajello, M., Allafort, A., et al., 2013, *ApJS*, 209, 34
- Ade, P. A. R., Aghanim, N., Armitage-Caplan, C., et al., 2013, submitted to *A&A*, arXiv:1303.5076v2
- Aharonian, F., Akhperjanian, A. G., Bazer-Bachi, A. R., et al., 2006, *Nature*, 440, 1018
- Albert, J., Aliu, E., Anderhub, H., et al., 2007, *Nucl. Instr. Meth. A*, 583, 494
- Aleksić, J., Alvarez, E. A., Antonelli, L. A., et al., 2012, *Astropart. Phys.*, 35, 435
- Aleksić, J., Ansoldi, S., Antonelli, L. A., et al., 2014a, *A&A*, 564, 5
- Aleksić, J., Ansoldi, S., Antonelli, L. A., et al., 2014b, *A&A*, 567, 135
- Archambault, S., Aune, T., Behera, B., et al., 2014, *ApJL*, 785, 16
- Atwood, W. B., Abdo, A. A., Ackermann, M., et al., 2009, *ApJ*, 697, 1071
- Baars, J. W. M., Genzel, R., Pauliny-Toth, I. I. K. and Witzel, A., 1977, *A&A*, 61, 99
- Band, D. L. & Grindlay, J. E., 1985, *ApJ*, 298, 128
- Barthelmy, S. D., Barbier, L. M., Cummings, J. R., et al., 2005, *Space Science Reviews*, 120, 143
- Bassani, L., Landi, R., Masetti, N., et al., 2009, *MNRAS*, 397, 55
- Baumgartner, W. H., Tueller, J., Markwardt, C. B., et al., 2013, *ApJS*, 207, 19
- Berger, K., Paneque, D. & Giavitto, G., 2010, in *Proc. 5th Texas Symposium on Relativistic Astrophysics, TEXAS2010 (SLAC-PUB-15014)*
- Berger, K., Giavitto, G., Lindfors, E., et al., 2011, in *Proc. Fermi Symposium*, C110509, arXiv:1110.6368v1
- Bloom, S. D. & Marscher, A. P., 1996, *ApJ*, 461, 657
- Burrows, D. N., Hill, J. E., Nousek, J. A., et al., 2005, *Space Science Reviews*, 120, 165
- Condon, J. J., Cotton, W. D., Greisen, E. W., et al., 1998, *AJ*, 115, 1693
- Dermer, C. D. & Schlickeiser, R., 1993, *ApJ*, 416, 458
- Domínguez, A., Primack, J. R., Rosario, D. J., et al., 2011, *MNRAS*, 410, 2556
- Edelson, R. A., & Krolik, J. H., 1988, *ApJ*, 333, 646
- Fazio, G. G., & Stecker, F. W., 1970, *Nature*, 226, 135
- Finke, J. D., Razzaque S., & Dermer, C. D., 2010, *ApJ*, 712, 238
- Fiorucci, M. & Tosti, G., 1996, *A&AS*, 116, 403
- Fitzpatrick, E. L., 1999, *PASP*, 111, 63
- Fomin, V. P., Stepanian, A. A., Lamb, R. C., et al., 1994, *Astropart. Phys.*, 2, 137
- Franceschini, A., Rodighiero, G. & Vaccari, M., 2008, *A&A*, 487, 837
- Fukugita, M., Shimasaku, K., & Ichikawa, T., 1995, *PASP*, 107, 945
- Gilmore, R. C., Madau, P., Primack, J. R., et al., 2009, *MNRAS*, 399, 1694
- Gould, R. J., & Schreder, G., 1966, *Phys. Rev. Lett.*, 16, 252
- Haefner, D., Schweizer, T., Dazzi, F. & Corti, D., 2011, in *Proc. 32nd ICRC Beijing*, 9, 246, arXiv:1111.1299v1
- Hauser, M. G., & Dwek, E., 2001, *ARA&A*, 39, 249
- Kneiske, T. M. & Dole, H., 2010, *A&A*, 515, A19

Krimm, H. A., Holland, S. T., Corbet, R. H. D., et al. 2013, ApJS, 209, 14

Li, T. & Ma, Y., 1983, ApJ, 272, 317

Lombardi, S., Berger, K., Colin, P., Ortega, A. D. & Klepser, S., 2011, in Proc. 32nd ICRC Beijing, 8, 183, arXiv:1109.6195v1

Mannheim, K. & Biermann, P. L., 1992, A&A, 253, 21

Maraschi, L., Ghisellini, G., & Celotti, A., 1992, ApJ, 397, 5

Mariotti, M., et al., 2010 (the MAGIC Collaboration) Atel#2753

Mattox, J. R., Bertsch, D. L., Chiang, J., et al., 1996, ApJ, 461, 396

Monet, D. G., Levine, S. E., Canzian, B., Ables, H. D., et al., 2003, AJ, 125, 984

Moralejo, A., Gaug, M., Carmona, E., et al., 2009, arXiv:0907.0943

Mücke, A., Protheroe, R. J., Engel, R., et al., 2003, Astropart. Phys., 18, 593

Nilsson, K., Pursimo, T., Heidt, J., et al., 2003, A&A, 400, 95

Nilsson, K., Pursimo, T., Takalo, L. O., et al., 1999, PASP, 111, 1223

Nolan, P. L., Abdo, A. A., Ackermann, M., et al., 2012, ApJS, 199, 31

Poole, T. S., Breeveld, A. A., Page, M. J., et al., 2008, MNRAS, 383, 627

Poutanen, J., Zdziarski, A. A. and Ibragimov, A., 2008, MNRAS, 1427, 389

Prandini, E., Bonoli, G., Maraschi, L., Mariotti, M. & Tavecchio, F., 2010, MNRAS, 405, 76

Prandini, E., Bonoli, G., Maraschi, L., Mariotti, M. & Tavecchio, F., 2011, in Proc. Cosmic Radiation Fields: sources in the early Universe, CRF2010, arXiv:1101.5005

Press, W. H., Teukolsky, S. A., Vetterling, W. T., & Flannery, B. P., 1992, *Numerical Recipes in C*, The Art of Scientific Computing, 2nd Edition

Richards, J., et al., 2011, ApJS, 194, 29

Rissi, M., PhD thesis, 2009, ETH Zurich, Diss. ETH No.18322

Roming, P. W. A., Kennedy, T. E., Mason, K. O., et al., 2005, Space Science Reviews, 120, 95

Sbarufatti, B., Treves, A., & Falomo, R., 2005, ApJ, 635, 173

Schlaflly, E. F. & Finkbeiner, D. P., 2011, ApJ, 737, 103

Schlegel, D. J., Finkbeiner, D. P., Davis, M., 1998, ApJ, 500, 525

Sérsic, J. L., 1968, *Atlas de galaxias australes*, Observatorio Astronomico, Cordoba

Shaw, M. S., Romani, R. W., Cotter, G., et al., 2013, ApJ, 764, 135

Sikora, M., Begelman, M. C., & Rees, M. J., 1994, ApJ, 421, 153

Stecker, F. W., 1969, AJ, 157, 507

Stecker, F. W., Malkan, M. A., & Scully, S. T., 2006, ApJ, 648, 774

Takami, H., 2011, MNRAS, 413, 1845

Tavecchio, F., Ghisellini, G., Ghirlanda, G., Foschini, L. & Maraschi, L., 2010, MNRAS, 401, 1570

Urry, C. M., & Padovani, P., 1995, PASP, 107, 803

Vaughan, S., Edelson, R., Warwick, R. S. & Uttley, P., 2003, MNRAS, 345, 1271

Zanin, R., PhD thesis, 2011, Universitat Autònoma de Barcelona

Zanin, R., Carmona, E., Sitarek, J., Colin, P., et al., 2013, in Proc. 33rd ICRC Rio de Janeiro, id773

¹ IFAE, Campus UAB, E-08193 Bellaterra, Spain

² Università di Udine, and INFN Trieste, I-33100 Udine, Italy

³ INAF National Institute for Astrophysics, I-00136 Rome, Italy

⁴ Università di Siena, and INFN Pisa, I-53100 Siena, Italy

⁵ Croatian MAGIC Consortium, Rudjer Boskovic Institute, University of Rijeka and University of Split, HR-10000 Zagreb, Croatia

⁶ Max-Planck-Institut für Physik, D-80805 München, Germany

⁷ Universidad Complutense, E-28040 Madrid, Spain

⁸ Inst. de Astrofísica de Canarias, E-38200 La Laguna, Tenerife, Spain

⁹ University of Łódź, PL-90236 Lodz, Poland

¹⁰ Deutsches Elektronen-Synchrotron (DESY), D-15738 Zeuthen, Germany

¹¹ ETH Zurich, CH-8093 Zurich, Switzerland

¹² Universität Würzburg, D-97074 Würzburg, Germany

¹³ Centro de Investigaciones Energéticas, Medioambientales y Tecnológicas, E-28040 Madrid, Spain

¹⁴ Technische Universität Dortmund, D-44221 Dortmund, Germany

¹⁵ Inst. de Astrofísica de Andalucía (CSIC), E-18080 Granada, Spain

¹⁶ Università di Padova and INFN, I-35131 Padova, Italy

¹⁷ Università dell'Insubria, Como, I-22100 Como, Italy

¹⁸ Unitat de Física de les Radiacions, Departament de Física, and CERES-IEEC, Universitat Autònoma de Barcelona, E-08193 Bellaterra, Spain

¹⁹ Institut de Ciències de l'Espai (IEEC-CSIC), E-08193 Bellaterra, Spain

²⁰ Japanese MAGIC Consortium, Division of Physics and Astronomy, Kyoto University, Japan

²¹ Finnish MAGIC Consortium, Tuorla Observatory, University of Turku and Department of Physics, University of Oulu, Finland

²² Inst. for Nucl. Research and Nucl. Energy, BG-1784 Sofia, Bulgaria

²³ Universitat de Barcelona, ICC, IEEC-UB, E-08028 Barcelona, Spain

²⁴ Università di Pisa, and INFN Pisa, I-56126 Pisa, Italy

²⁵ now at: NASA Goddard Space Flight Center, Greenbelt, MD 20771, USA and Department of Physics and Department of Astronomy, University of Maryland, College Park, MD 20742, USA

²⁶ now at Ecole polytechnique fédérale de Lausanne (EPFL), Lausanne, Switzerland

²⁷ now at Department of Physics & Astronomy, UC Riverside, CA 92521, USA

²⁸ now at Finnish Centre for Astronomy with ESO (FINCA), Turku, Finland

²⁹ also at INAF-Trieste

³⁰ also at Instituto de Física Teórica, UAM/CSIC, E-28049 Madrid, Spain

³¹ now at: Stockholm University, Oskar Klein Centre for Cosmoparticle Physics, SE-106 91 Stockholm, Sweden

³² now at GRAPPA Institute, University of Amsterdam, 1098XH Amsterdam, Netherlands

³³ INAF Istituto di Radioastronomia, 40129 Bologna, Italy

³⁴ Dipartimento di Fisica e Astronomia, via Ranzani 1, 40127 Bologna, Italy

³⁵ Cahill Center for Astronomy and Astrophysics, California Institute of Technology, 1200 E California Blvd, Pasadena, CA 91125

³⁶ Isaac Newton Institute of Chile, St. Petersburg Branch, St. Petersburg, Russia

³⁷ Pulkovo Observatory, 196140 St. Petersburg, Russia

³⁸ Astronomical Institute, St. Petersburg State University, St. Petersburg, Russia

³⁹ National Radio Astronomy Observatory, PO Box 0, Socorro, NM 87801

⁴⁰ Agenzia Spaziale Italiana (ASI) Science Data Center, I-00133 Roma, Italy

⁴¹ Department of Physics, Purdue University, 525 Northwestern Ave, West Lafayette, IN 47907

⁴² Department of Physics and Mathematics, College of Science and Engineering, Aoyama Gakuin University, 5-10-1 Fuchinobe, Chuo-ku, Sagami-hara-shi Kanagawa 252-5258, Japan

⁴³ University of Missouri-St. Louis, St. Louis, Missouri, USA

⁴⁴ Physics Department, California Polytechnic State University, San Luis Obispo, CA 94307, USA

⁴⁵ Deceased

⁴⁶ * Corresponding authors: Kazuhito Kodani (kodanik.z@gmail.com), David Paneque (dpaneque@mppmu.mpg.de), Josefa Becerra González (jbecerragonzalez@gmail.com)

Appendix A: *Swift*-XRT and *Swift*-UVOT results

Table A.1. Results of *Swift*-XRT observation during MWL campaign 2010; observation start time (MJD); integral flux in the energy range between 0.3 and 2 keV; integral flux in the energy range between 2 and 10 keV; power-law photon index, and reduced chi-square χ^2_ν with the number of degree of freedom n_{dof} .

Observation date	MJD [days]	Flux (0.3 – 2 keV) [10^{-12} erg/cm ² /s]	Flux (2 – 10 keV) [10^{-12} erg/cm ² /s]	photon index (0.3 – 10 keV)	χ^2_ν	n_{dof}
July 7	55384.044	1.0 ± 0.1	0.9 ± 0.3	2.0 ± 0.6	0.2	1
July 8	55385.048	1.9 ± 0.1	0.6 ± 0.2	2.5 ± 0.5	0.8	2
July 11	55388.803	1.8 ± 0.1	0.6 ± 0.2	2.5 ± 0.6	1.1	3
July 16	55393.031	7.1 ± 0.1	1.2 ± 0.2	2.9 ± 0.2	1.1	13
July 20	55397.047	4.3 ± 0.1	0.9 ± 0.2	2.8 ± 0.3	1.0	7
July 29	55406.818	15.2 ± 0.1	5.8 ± 0.4	2.5 ± 0.1	0.7	36
Aug. 5	55413.024	7.3 ± 0.1	1.2 ± 0.3	3.0 ± 0.4	1.0	7
Aug. 10	55418.049	1.8 ± 0.1	0.8 ± 0.2	2.3 ± 0.4	1.3	3
Aug. 22	55430.218	1.3 ± 0.1	0.6 ± 0.3	2.3 ± 0.7	0.4	1
Sep. 1	55440.594	4.9 ± 0.1	0.7 ± 0.2	3.0 ± 0.4	0.4	4
Sep. 8	55447.090	1.7 ± 0.1	0.7 ± 0.2	2.4 ± 0.4	0.7	3
Sep. 12	55451.852	3.5 ± 0.1	1.7 ± 0.2	2.3 ± 0.2	1.5	10
Sep. 18	55457.194	4.5 ± 0.1	1.5 ± 0.3	2.5 ± 0.3	1.3	8

Table A.2. Results of *Swift*-UVOT observation during MWL campaign 2010, observation start time (MJD), and fluxes for the different three UV filters.

Observation date	MJD [days]	UV W1 flux [10^{-11} erg/cm ² /s]	UV M2 flux [10^{-11} erg/cm ² /s]	UV W2 flux [10^{-11} erg/cm ² /s]
July 5	55382.995	1.8 ± 0.2	3.8 ± 0.5	2.7 ± 0.2
July 7	55384.046	1.5 ± 0.1	3.1 ± 0.3	1.9 ± 0.2
July 8	55385.049	1.4 ± 0.1	2.9 ± 0.3	2.3 ± 0.2
July 11	55388.808	1.2 ± 0.1	2.7 ± 0.2	1.9 ± 0.1
July 16	55393.035	1.8 ± 0.2	2.6 ± 0.3	2.5 ± 0.2
July 20	55397.051	1.6 ± 0.1	3.8 ± 0.3	2.8 ± 0.2
July 29	55406.842	2.5 ± 0.1	5.2 ± 0.3	4.6 ± 0.2
Aug. 5	55413.026	2.5 ± 0.1	5.0 ± 0.4	3.8 ± 0.2
Aug. 10	55418.075	1.8 ± 0.1	3.4 ± 0.3	3.0 ± 0.2
Aug. 16	55424.063	2.1 ± 0.3	3.7 ± 0.6	2.1 ± 0.3
Aug. 22	55430.223	1.3 ± 0.1	2.6 ± 0.2	2.1 ± 0.1
Sep. 1	55440.595	2.5 ± 0.1	4.6 ± 0.3	4.0 ± 0.2
Sep. 8	55447.091	1.6 ± 0.1	2.9 ± 0.2	2.3 ± 0.2
Sep. 12	55451.851	1.7 ± 0.1	3.0 ± 0.2	2.5 ± 0.2
Sep. 18	55457.197	2.1 ± 0.1	4.3 ± 0.3	3.4 ± 0.2